Felix Linhardt, BSc.

Ao.Univ.Prof. Dr. Martin Gröschl

TECHNISCHE UNIVERSITÄT WIEN
Vienna | Austria

DIPLOMARBEIT

Simultane Messungen von Schall, Vibration und Strömung, sowie Bestimmung von Schallübertragungsfunktionen im Kontext von Luft-Wasser-Wärmepumpen

Ausgeführt am

Institut für Angewandte Physik
der Technischen Universität Wien

unter der Anleitung von

Ao.Univ.Prof. Dr. Martin Gröschl

in Zusammenarbeit mit

DI Dr. Christoph Reichl

am

Austrian Institute of Technology

durch

Felix Linhardt, BSc.
Weißgerberlände 38/28
A-1030 Wien

Wien, am 4. Februar 2018

Simultaneous measurements of sound, vibration, and flow, as well as determination of acoustic transfer functions in the context of air water heat pumps

Abstract

Air-to-water heat pumps provide numerous ecological and economical gains, but the associated noise emissions proved to be problematic. The aim of this thesis was to create a measurement system for simultaneous detection of sound, vibration and air flow, to aid the development of quieter heat pumps. The system was used on a commercially available heat pump and several ways of data evaluation and visualization have been described. Transfer functions of acoustic absorber materials and air-side heat exchangers were measured, and the effects of air flow on these transfer functions were investigated.

This thesis was carried out at the Austrian Institute of Technology (AIT), in the context of the SilentAirHP project.

Zusammenfassung

Luft-Wasser-Wärmepumpen haben zahlreiche ökologische und ökonomische Vorteile, jedoch sind die damit verbundenen Lärmemissionen problematisch. Ziel dieser Arbeit war der Aufbau eines Messsystems zur simultanen Erfassung von Schall, Vibration und Luftströmung, um damit die Entwicklung leiserer Wärmepumpen zu unterstützen. Das System wurde an einer kommerziell erhältlichen Wärmepumpe praktisch angewandt, und mehrere Arten der Datenauswertung und -visualisierung wurden beschrieben. Übertragungsfunktionen von akustischen Absorbermaterialien und luftseitigen Wärmetauschern wurden gemessen, und die Effekte der Luftströmung auf diese Übertragungsfunktionen wurden untersucht.

Diese Arbeit wurde im Kontext des SilentAirHP Projekts am Austrian Institute of Technology (AIT) ausgeführt.

Acknowledgements

First I would like to extend my gratitude to my advisor, Prof. Martin Gröschl, who showed both, patience and flexibility. His guidance was of great value when facing the challenges associated with a master's thesis.

Further, I want to thank all AIT staff members and fellow students around the SilentAirHP project for the great time I had at the AIT:
Christoph Reichl, Johann Emhofer, Christian Köfinger, Andreas Zottl, Andreas Kotal, Wolfgang Zach, Lothar Büscher, Peter Petschovitsch, Karoline Alten, Peter Wimberger, Norbert Schmiedbauer, Elisabeth Wasinger, David Meisl, Raimund Zitzenbacher, Anna-Maria Sumper, and Thomas Fleckl. Christoph, I really enjoyed our sometimes unconventional business hours.

Far beyond this thesis, I am very grateful for my family's continued support on all matters of life – especially on days, when "writing is not fun".

Amongst all others who made this thesis happen, I want to thank all contributors of open source software. Especially Python, NumPy, SciPy and Matplotlib are a very important part of my toolbox since many years, and LaTeX makes this thesis look pretty.

Felix Linhardt

Vienna, 4th February 2018

Contents

1 Introduction

Heat pumps are a hot topic in recent years. As the fact becomes more and more accepted [1], that climate change needs to be addressed, conservation and efficient use of energy grows ever more important.

Heat pumps work by using external energy to move thermal energy from a lower level reservoir to a higher level reservoir. This is the opposite to what would happen, if the system was left on its own, and purely followed the second law of thermodynamics.

An application of heat pumps within everyone's field of experience is the refrigerator. It takes thermal energy from the cold side (inside the fridge) and moves it to its warmer surroundings (the kitchen). This work is accomplished by the use of electricity. The same mode of operation also applies to heat pumps for domestic heating purposes: From the already cooler outside environment, further thermal energy is removed and added to the house's interior.

The environmental costs of operation of heat pumps depend to a high degree on the clean generation of electricity. But even with coal as a "dirty" source of electricity, heat pumps are able to provide some ecological gain. The average efficiency of a typical coal power plant in Germany (2010) is around 35-38% [2]. The coefficient of performance (COP) of modern heat pumps is above 3.5 [3]. So, even when using coal as primary energy source, the conversion to electrical power and use of an heat pump still results in an energy gain, and therefore CO_2 reduction, compared to direct coal firing. This calculation does not even include the benefits of far better exhaust gas cleaning processes in centralized firing facilities.

An *air water* heat pump uses air as thermal source and water as thermal sink. In the context of domestic heating, this would be the outside air as source and the water cycle of the heating system as sink.

The environmental air is a very appealing source of energy, as it is readily available without further infrastructural efforts. An other possible thermal source would be geothermal energy - but this comes with the associated need for ground heat exchangers: drilled vertical which tends to be expensive and subjected to regulations, or horizontal which needs a large land area. Air as heat source circumvents these problems, at the price of a slightly lower efficiency and more noise.

Noise is particularly problematic in densely populated areas - coinciding with the areas where ground source heat pumps are especially difficult to integrate. In modern air water heat pumps, there are two main sources of primary vibration and noise: The fan which moves the air over the heat exchanger and the compressor which drives the refrigerant cycle.

Depending on the design of the heat pump, these components affect different parties. In the split system design the compressor is usually contained in an indoor unit, primarily affecting the residents of the building where the heat pump is installed, whereas the fan is in the outdoor unit, affecting the building's residents and possible neighbors in the vicinity. In the self contained design all major components are housed in the outdoor unit, removing the compressor from the building, but adding further noise to the surrounding areas.

Steady random noise can easily be ignored by the human brain, as long as the total level lies within certain limits. Abrupt or intermittent sounds have a much higher potential of psychoacoustic annoyance [4]. This is also a very important fact for the acoustic optimization of heat pumps: Some components like expansion valves tend to exhibit very short-timed signatures in their acoustic characteristics.

Another very sudden change in the acoustic emission occurs in defrosting phases. When the air passes through the heat exchanger it usually dips below the dew point. At low temperatures the condensed water freezes and a layer of ice forms on the heat exchanger. This impedes heat transfer and obstructs air flow, which makes periodic defrosting procedures necessary [5]. These deicing procedures usually consist of powering down the heat pump and reversing the refrigerant cycle to rapidly melt the ice off. Afterwards, the heat pump has to power down again, reverse back to its original working direction and resume normal operation. This strongly interrupts the heat pump's usual soundscape and increases its noticeability.

Noise emission is a major factor that could hamper the widespread adoption of air water heat pumps. Strict regulations regarding noise emission together with an increasing market [6] for air water heat pumps put pressure on heat pump manufacturers to develop new models to meet these demands. Pressure to innovate and compete also leads to heat pumps that more efficiently extract the thermal energy from the surrounding air. This overall development has beneficial side-effects for both people and environment.

2 Goals of this thesis

At the time of writing this thesis, the *Silent Air Heat Pump* project (SilentAirHP[1]) [7] is an ongoing research project at the Austrian Institute of Technology (AIT). Primary goal is to evaluate and improve noise reduction measures for air water heat pumps. This includes the construction of a modular heat pump prototype for testing of individual components, control patterns and noise reduction measurements, or combinations thereof.

Other examples of activities within SilentAirHP include studies on the use of active noise canceling (ANC) [8] in heat pump construction, the survey of heat pump prototypes with an acoustic camera [9], and further approaches with numerical simulations. The results of this project will be distributed to heat pump manufacturers to improve product development.

This thesis was conducted in the context of the SilentAirHP project. In the course of this thesis two main aspects were addressed:

The first objective was to create a system for simultaneous measurements of acoustic, vibration and air flow signals. This provides a quick way for an in-depth evaluation of structural changes in heat pump prototypes.

The second objective was to use this system in a practical scenario, and to measure acoustic transfer functions needed by other branches of the SilentAirHP project.

[1]The Climate and Energy Fund (KLI.EN) and the Austrian Research Promotion Agency (FFG) are gratefully acknowledged for funding the SilentAirHP project under Grant No. 848891. The project is supported in the framework of the 1st call "Energieforschung".

3 Measurement system

3.1 Requirements

For the intended use as a tool for "investigative diagnostics", several channels for audio and vibration signals were needed. The sampling frequency had to meet or exceed 40 kHz per channel to enable recording audio signals over the full frequency range of the human hearing capability.

Additional channels were needed to pick up the voltage-based signals of a CTA bridge and other additional equipment. Output channels further expand the scope of possible applications.

Inter-channel timekeeping of the measurement process was also important as this allows to study correlations and time shifts down to sampling interval level.

3.2 Hardware

The measurement system's hardware was selected in a modular approach. Each sensor has its own amplifier or self-contained subunit of an amplifier, which forwards the signal to a National Instruments USB-6251 unit, where digitalization takes place. This way, each sensor and amplifier can be exchanged independently, without any changes in the data acquisition stage. A centralized multichannel digitalization unit also carries the advantage of very simple time relations between the single channels.

The interface of the USB-6251 unit was wired to provide 11 input channels. 6 channels via BNC, 4 via 6.35 mm phone connectors, one via banana plugs. For output, there were two additional channels, wired with cinch connectors. This configuration proved to be useful for most of our measurement needs:

- The four phone connector inputs were used for audio signals. Amplification was done with the four independent pre-amplifiers of a readily available Mackie 1202-VLZ3. The microphones were four MicW M215 class 1 measurement microphones which were supplied with phantom power by the Mackie device.
- Four BNC connectors were reserved for vibration signals. The four DEWETRON DAQP-Charge-A devices amplified the signals generated by Brüel & Kjær charge accelerometers, type 4370.

- The remaining two BNC connectors were connected to the constant temperature anemometry (CTA) unit, a DANTEC model 56C17. One channel measured the raw signal, and the other channel received a 100 Hz high pass filtered signal via a DANTEC 56N20 signal conditioner. Apart from first tests and calibrations, all measurements were carried out with the unfiltered channel.
- The multi purpose input channel with banana connectors was primarily used with a pressure sensor which has an integrated amplifier, so no extra amplification was necessary. This channel was only used for calibrating the CTA probe and was not part of any measurement ensemble, that is why it is not represented in figure 1.
- Finally, the two cinch output lines went through a Pioneer A-337 amplifier, to two Pioneer TS-G1749 speakers.

3.3 Software

The digitalization process of the measured signal takes place in the National Instruments data acquisition unit. This unit needs the NI DAQmx drivers for communication, which expose a C/C++ API. The PyDAQmx module contains a full Python interface to this API [10]. From this point on, the task of controlling the measurement system can be done in pure Python, which opens the path to a convenient interactive work-flow, using IPython.

As part of this thesis, a Python library was written, which enables the user to efficiently conduct simple measurements, without having to deal with the complex task-based model of the DAQmx driver and pyDAQmx. Several measurement scenarios are predefined and can easily be extended. For data storage the *.npz format was chosen. It is part of the NumPy package and has an open specification [11].

Python 2.7 and 3.x are equally suited for use with pyDAQmx and our library. But, even though working on both 32 and 64 bit, the use of 32 bit hardware and software imposes some restrictions on memory consumption and array length, which limits the maximum recording time.

3.4 Calibration

The NI USB-6251 unit comes factory-calibrated with regular recalibration intervals. It is not primarily designed for acoustics, and most specifications

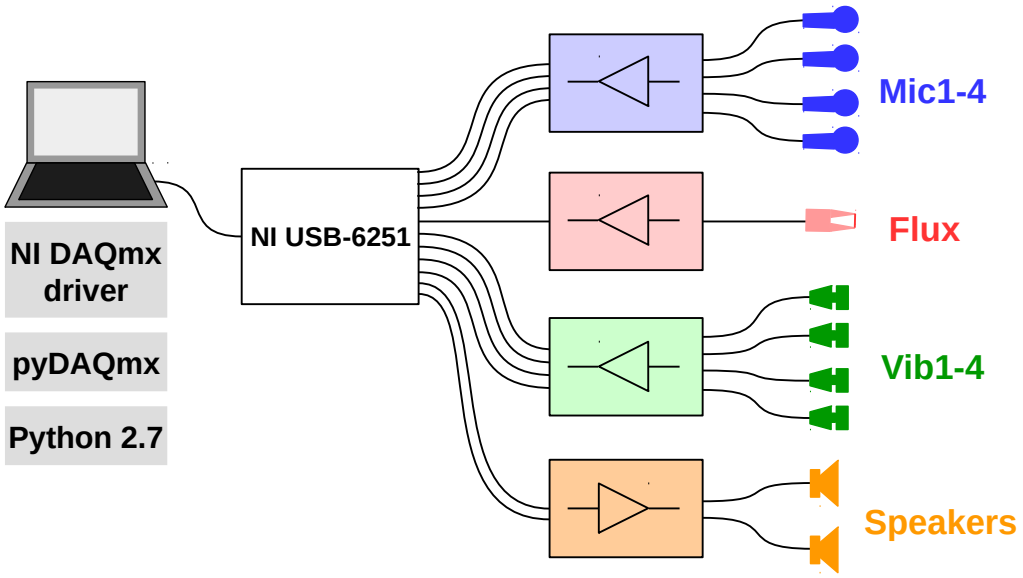

Figure 1: *Measurement system and software stack.*

greatly exceed the requirements - up to 1.25 MHz sampling rate and an exceptionally flat frequency response curve with -0.5 dB at 500 kHz.

3.4.1 Acoustics

As the Mackie 1202-VLZ3 is not designed for scientific use, detailed information about its preamplifiers is rather sparse. Through the complete system from mic input to any output, the frequency response for the range of 20 Hz to 60 kHz is given with +0/-1 dB, and -3 dB at 100 kHz [12]. In the technical specification sheet of the similar Mackie 1202-VLZ PRO the same frequency response is listed, but also values for the preamplifiers alone are given: 5 Hz - 100 kHz at -1 dB and 3 Hz - 192 kHz at -3 dB [13]. This can be seen as a hint towards a flatter curve for the preamplifiers compared to the complete system for the 1202-VLZ3 device. The preamplifier's total gain can be adjusted via a knob, but it is not possible to select specific values.

The MicW M215 microphones come with a detailed calibration report, providing the frequency response values for the 20 Hz to 20 kHz range in $1/6^{\text{th}}$ octave resolution. The sensitivity information is also given, but has not been used, as the amplification gain of the Mackie device is not known.

To complete the information needed for the acoustic measurement chain, a

Brüel & Kjær Type 4231 Sound Calibrator device was used. It is directly attached onto each microphone and emits a 1 kHz sine tone at 93.98 dB_{SPL}, which equates to a sound pressure of 1 Pa root mean square. Note that by convention weighting curves (A-D, Z, ITU-R 468, ISO 226) are defined to have unity value at 1 kHz - this way the calibrator's value is exact, regardless of the chosen weighting. By recording this reference signal, a calibration factor can be calculated for each microphone to convert the measured signal from volt to pascal. This procedure has to be repeated each time the system is set up, or when the gains on the Mackie device were changed.

3.4.2 Vibration

The Brüel & Kjær Type 4370 vibration sensors are piezoelectric devices that produce a charge, proportional to the acceleration. The frequency response curve is flat for the most part of the spectrum, but exhibits a resonance peak at 16 kHz. The recommended upper frequency limit is defined with a 10% increase of the response function towards the resonance peak and is located at 4.8 kHz. Each sensor's sensitivity, which is usually around 10 $pC/(m/s^2)$, is given in its calibration certificate. Recalibration is done by the manufacturer in regular intervals. The DEWETRON amplifier is also re-calibrated regularly and has a frequency range (-3 dB) of 0.1 Hz to 50 kHz which well exceeds our targeted range.

As all parts of the vibration measurement chain are calibrated by the respective companies, the process of obtaining meaningful values is simple. The fixed factor of the charge amplifier is multiplied with the measured voltage signal and each sensor has its individual conversion factor which is also applied by a simple division. The result is a signal given in m/s^2.

3.4.3 Air flow

The DANTEC 56C17 CTA unit delivers a signal, which corresponds to the heating voltage of the hot-wire probe. The conversion from voltage to an air velocity in m/s is found via calibration.

The calibration device consists of a pressurized cavity and a nozzle, creating a free jet of air, where the probe is placed. Due to the low pressures and velocities involved (< 200 Pa, < 18 m/s), air can be assumed incompressible, and Bernoulli's equation can be used. This allows to calculate the air velocity from the air pressure within the cavity.

The relation of voltage and velocity is modeled (see [14]):

$$U^2 = A + B \cdot u^{0.5} \tag{1}$$

U	...	hot-wire voltage
A, B	...	calibration coefficients
u	...	flow speed

Pairs of measured pressure (leading to air velocity) and measured probe signal can then be used to determine the calibration coefficients A and B, leading to the transfer function of the CTA measurement chain.

3.4.4 Output

Accuracy or linearity of the transfer functions were regarded to be of secondary importance for the output channels. The idea was to measure different setups, and compare the measurements afterwards (e.g. transfer function with / without acoustic absorber; see chapter 6). Key for this application is the repeatability of the output signal.

4 Examination of a commercially available heat pump

The contents of this chapter were also presented at the DAGA 2017 [18].

4.1 Objectives

Aim of this measurement campaign was to demonstrate an efficient way to measure and analyze acoustic, vibration, and air flow data from a commercial heat pump. This would enable heat pump manufacturers to evaluate the effects and benefits of structural changes to their prototypes in a time effective manner.

A secondary goal was to evaluate the possible use of vibration or acoustic sensors for continuous machine health monitoring. This includes measuring and comparing acoustic and vibrational signatures of different operational states, as well as monitoring transient events.

4.2 Setup

The setup was housed in the climate chambers of the *ENERGYbase* building at the Austrian Institute of Technology.

Due to the heat pump being a split device, both climate chambers were in use. The outdoor unit's chamber was put to several defined climate conditions. The generated heat was then transferred to a water circuit and cooled away by a thermal sink. Each outside climate condition was measured for four different power settings of the heat pump: 20% as the lowest allowed setting, 38% which corresponds to the heat pump's nominal power rating, and keeping equal stepping, at 69% and 100%. The indoor unit, which houses the compressor and the water-side heat exchanger, has a large front door which can be unhinged easily. To simulate a 'structural change', similar to a manufacturer heavily modifying a prototype, each power/climate setting was measured with and without the indoor unit's front door.

4.2.1 Heat pump

The surveyed heat pump is a split device with a nominal heating power of 5 kW. The indoor unit houses the compressor, the control unit, all power electronics and a water tank for hot water preparation. During the measurements, this tank was filled up with water to prevent resonances.

The outdoor unit was connected to the indoor unit via two copper pipes for forward and return flow of the refrigerant, and an electrical line providing power and signaling for valves and the fan.

4.2.2 Sensors

As part of our experimental setup, nine sensors were placed. These do not include humidity, temperature and water flow sensors, as these are part of the climate chamber's infrastructure.

Sensor	**HP unit**	**description**
Mic1	outdoor	front, not in direct air flow
Mic2	indoor	90 degree left of HP
Mic3	indoor	45 degree left of HP
Mic4	indoor	front of HP
Flux	outdoor	front, lower third unit height
Vib1	indoor	coolant valve, near compressor
Vib2	indoor	front door, inside
Vib3	indoor	floor plate, inside
Vib4	indoor	left side wall, outside

Description of sensor positions. Also see figure 2 for a graphical representation of the sensor placement.

Unlike previous tests with a sampling rate of 96 kHz, all sensors were sampled with 48kHz, allowing for longer measurements (see chapter 3.3), but still satisfying the Nyquist–Shannon sampling theorem for frequencies up to 24kHz.

4.3 Acoustic environment

The ENERGYbase climate chambers are acoustically optimized, but this does not lead to a zero background signal. There are several internal and external noise sources that create a background soundscape. Two kinds of

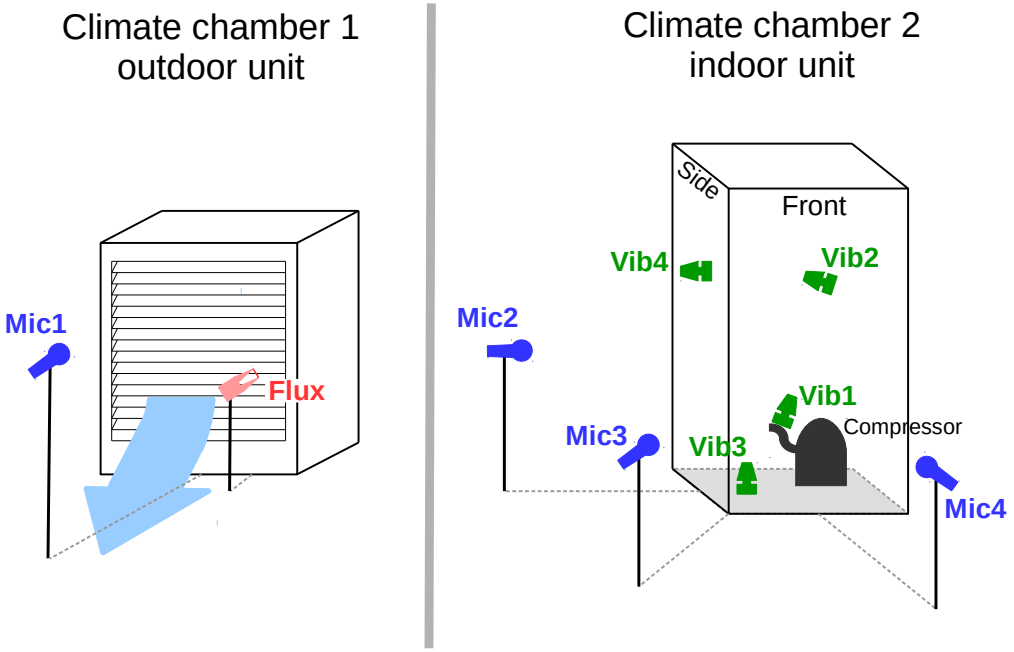

Figure 2: *Sensor placement on the heat pump. Sensor Vib2 is on the inside of the front door. The orientation of the climate chambers relative to each other is not accurately depicted.*

background can be observed: First, the background noise that remains when completely shutting down the heat pump. Second, when further shutting down the secondary water cycle and the climate chamber's air conditioning system. This leads to a further reduction of up to fifteen decibel in the frequency range below 100 Hz.

The background noise including climatisation is important as it may hinder measurements at very low levels. Figure 3 shows that for a measurement with closed-door and 38%-power conditions all major peaks have more than 15 dB distance to the background signal in the respective frequency range. Also the broadband portions of the signal stay for most parts well above the background.

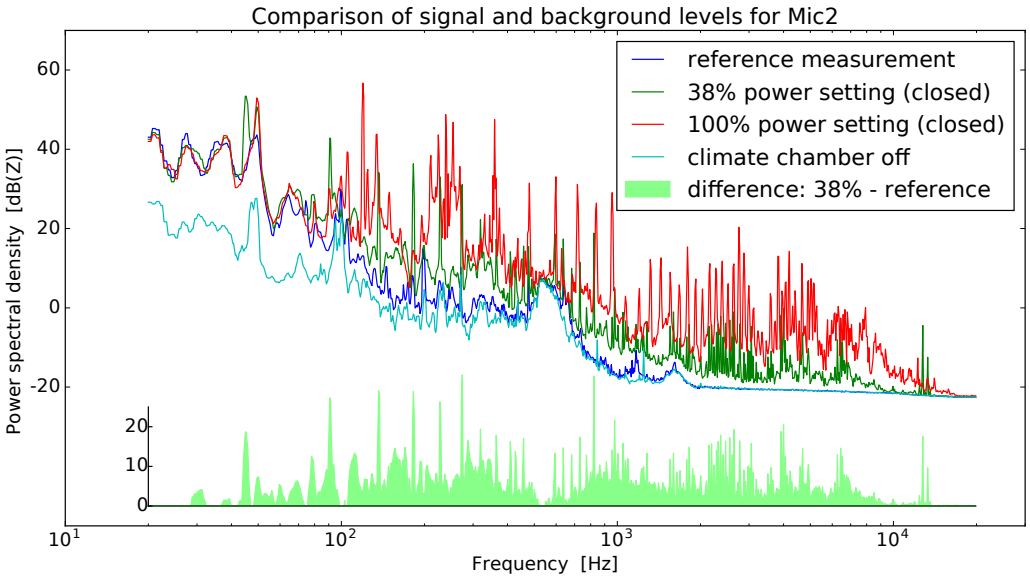

Figure 3: *Comparison of 38%/100% power settings and the reference measurement with the heat pump turned off. The green insert shows the dB-difference between one 38% measurements and the reference signal. All major peaks are more than 10 dB above the background.*

4.4 Data analysis

4.4.1 Time averages

A first and very simple approach is to examine time average values for each measurement and each sensor. One such quantity for acoustic sensors is the sound pressure level $L_{p/20\mu Pa}$. When using Z-weighting (also known as "zero", "flat" or no weighting), the calculation simplifies to a decibel conversion of the sound pressure signal's RMS value. If not further denoted, all levels are in $dB_{SPL}(Z)$.

For the vibration sensors, the root mean square of the vibration velocity was chosen as the characteristic value.

The constant temperature anemometer (CTA) signal is evaluated as RMS, indicating wind speed, and as standard deviation, indicating the air flow's turbulence.

Plotting

One measurement can be interpreted as a dot in a high dimensional space. Each sensor's time average value gives one coordinate, other conditions such as the heat pump's power setting or configurational/environmental parameters add coordinates in further dimensions.

A typical four-dimensional slice of this space can be seen in figure 4. Values for sensors Mic4 and Vib3 are represented as spacial coordinates, the dimension of power settings is color coded, and the different marker styles indicate the position of the heat pump's front door.

The system's overall behavior in figure 4 goes very well with what one might expect. Increasing the power setting leads to increased vibrations on the floor plate. It also leads to increased sound levels. The position of the front door seems to have no impact on the floor plate's vibration. But opening the font door greatly increases the sound level of Mic4, which is placed directly in front of the heat pump.

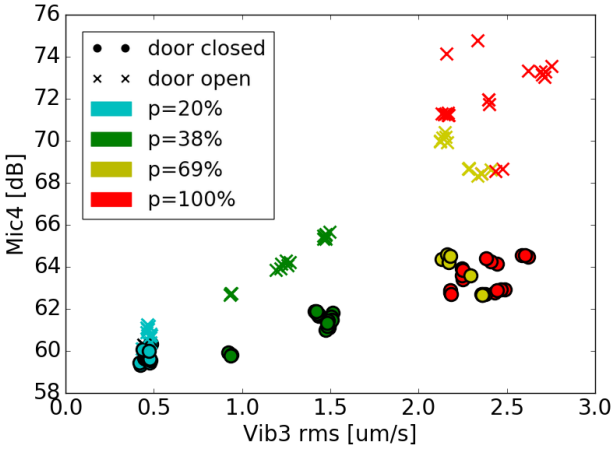

Figure 4: *Mic4 (indoor unit, front) vs. Vib3 (indoor unit, floor plate). There is a high correlation between the RMS value of the vibration, the decibel of the acoustic signal, and the heat pumps power setting. As well as the acoustic dampening by the closed front door, this behavior meets all expectations.*

Vibrational coupling

The left part of figure 5 shows the usual increase in vibration and sound level for increased power settings. A notable exception to this scheme are the closed-door measurements at the 38% power setting. The vibration value

of the heat pump's side panel are exceptionally high, and the sound level of Mic2, which is directly facing this panel, is not lower with the door closed.

This shows that the structural modification of installing a front door also creates new vibrational coupling paths. A detailed study of the spectra is shown in figure 6.

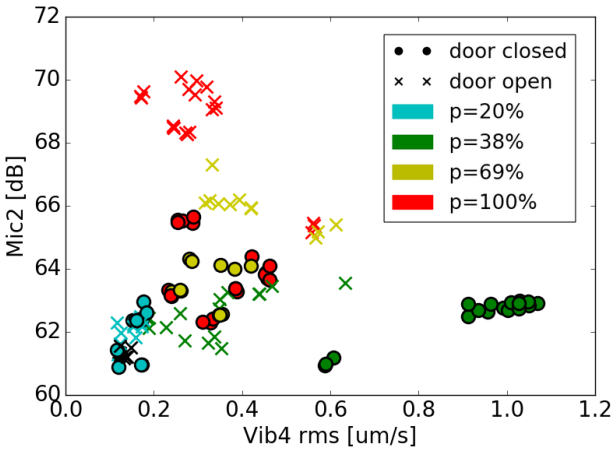

Figure 5: *Mic2 (indoor unit, left side) vs. Vib4 (indoor unit, left side). The measurements at the 38% setting with the front door closed show a remarkably high vibration value.*

Icing

The CTA sensor and Mic1 were located around the outdoor unit. Their values are shown in figure 7. Very noticeable is a group of measurements at the 38% power setting with high turbulence and sound levels, but very low mean air speed.

Further investigation in the metadata records shows, that these measurements were all conducted shortly before automatic de-icing procedures started. Therefore, a thick layer of ice has already built up on the heat exchanger, impeding air flow and thermal conductivity. In these situations, the fan creates more turbulence than flow, which leads to increased noise levels.

Figure 7 also shows groups of 2-3 points in the 69% and 100% power regime with high noise and turbulence values, but wind speed is not as low as for the afore mentioned 38% measurements. These points were recorded at very low temperature settings of the outdoor chamber, also shortly before auto-

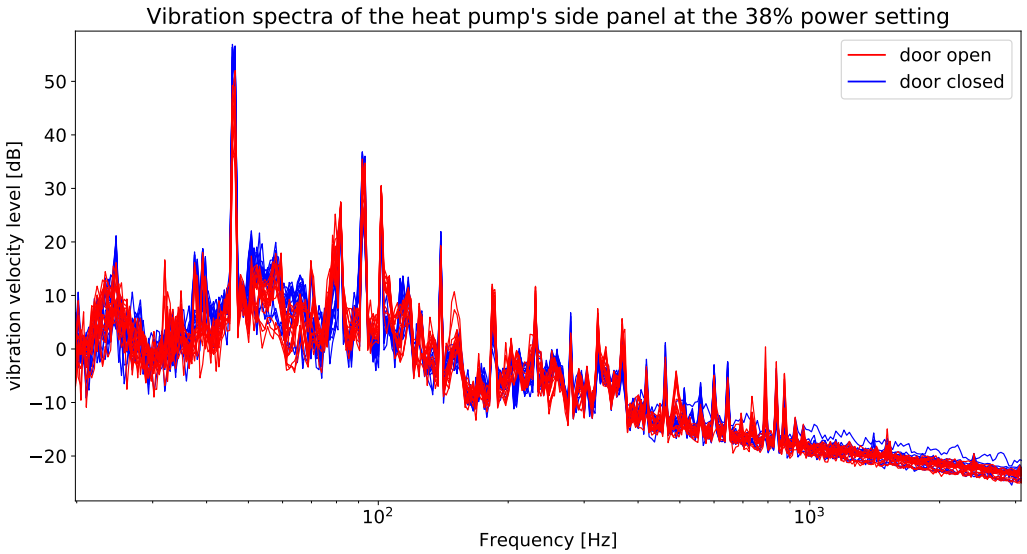

Figure 6: *Spectra of Vib4 (side panel). When the heat pump's front door is closed, the resonance peak at 45 Hz is 6 dB higher compared to the open door setting. A rise of about 3 dB can be seen at its harmonics at 90, 135 and 270 Hz.*

matic de-icing procedures. Compared to the 38% measurements, the de-icing started earlier, due to the high thermal demand at high power settings.

4.4.2 Cross correlation

Calculating the correlation of two signals for different time shifts Δt leads to the cross correlation function. The search for the maximum of the cross correlation function can therefore be interpreted as the search for the maximum similarity value of two signals with an unknown time shift between them. Doing so for each pair of sensors of one measurement, leads to the "cross correlation matrix" of this measurement. This matrix is symmetric, with ones at the diagonal, as each signal fully correlates with itself.

To prevent any bias from the measurements absolute values, the signals are normalized. This leads to the signals shape being the sole criterion for similarity. The aforementioned value of 1 for each signal's self-correlation is a direct result of this normalization.

Figure 8 shows two cross correlation matrices for the 69% power setting. Difference between them is the configuration of the heat pump's front door.

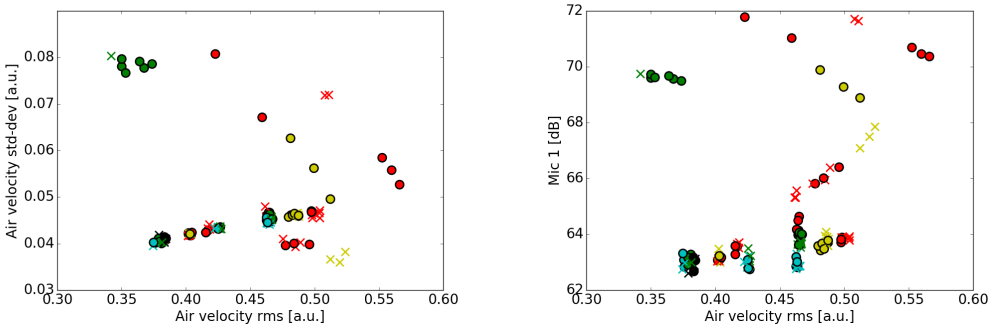

Figure 7: *Metadata shows, that all measurements with exceptionally high sound levels at Mic1 and high air flow turbulence (standard deviation of the CTA probe's signal) were taken shortly before automatic de-icing procedures started.*

Several observations can be made:

- The CTA signal does not correlate with any other signal. This is due to the fact, that this signal strongly resembles a DC signal with white noise on top - all other signals are rather periodic.
- Closing the door reduces the correlation between Vib1, Vib3 (floor plate and compressor valve) and the microphones Mic2-4.
- Mic1, located in the outdoor chamber, does not correlate with other signals.
- When the door is unhinged and leaned slightly against the right side of the heat pump, Vib2 (on the inside face of the door) retains some of its correlation with other Vib sensors.

Calculating the correlation value between fourier transforms of the sensor signals, one can construct a matrix analog to the cross correlation matrix. In time domain the value of Δt has to be stepped through. In the frequency domain, when discarding the phase information of the FFTs, no stepping has to be performed, and the direct correlation value may be used. Even though these two ways of calculating a matrix are very different, the results are rather similar.

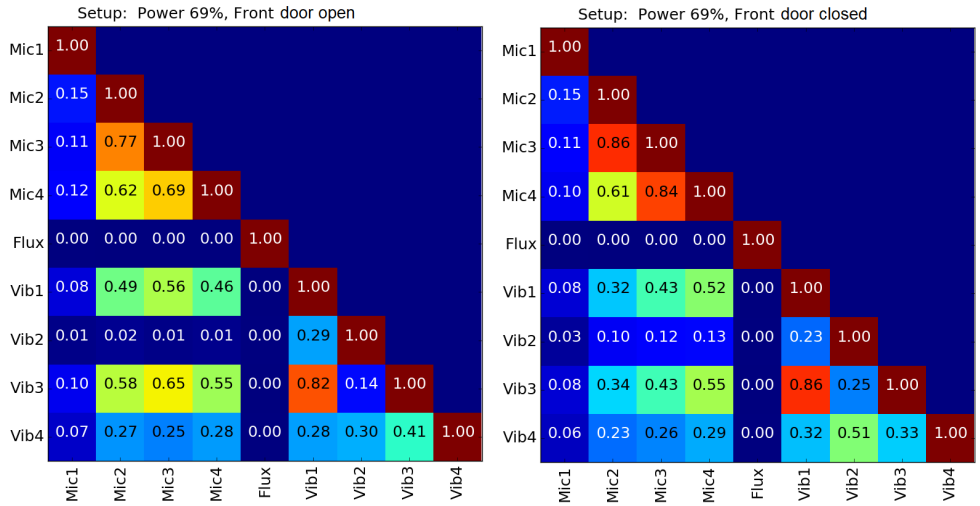

Figure 8: *Average cross correlation matrix for the 69% power setting. Left for open front door configuration, right matrix for closed front door. These matrices are symmetric, therefore the upper half was not calculated.*

4.4.3 Transient spectral events

Transient acoustic events are of very high interest. In some cases an event is clearly audible for bystanders, even though it does not significantly increase the overall decibel level measured. A more in-depth approach to evaluation of such a signal is a waterfall diagram. The data is split into small sections, each of them is fast fourier transformed, and the resulting spectra are printed as color coded strips, side-by-side. The result is a 2D image, showing the development of the spectrum over time.

One example of a waterfall diagram is shown in figure 9. It depicts the action of the heat pump's four way valve, while switching directions for the de-icing process. Clearly visible are the broadband signals of the click when starting the valve's movement, the hissing noise of the expanding refrigerant, and at the 1.9 s mark the click concluding the valve's action. A signature like this can be easily used by an automatic machine health monitoring system to confirm the valve's operation. Figure 9 shows in its upper and lower half the same signal from two different sensors, one vibration, one acoustic. The event is equally recognizable in both signals, making both sensors suitable for this monitoring task.

Comparing different waterfall diagrams creates an additional way of identify-

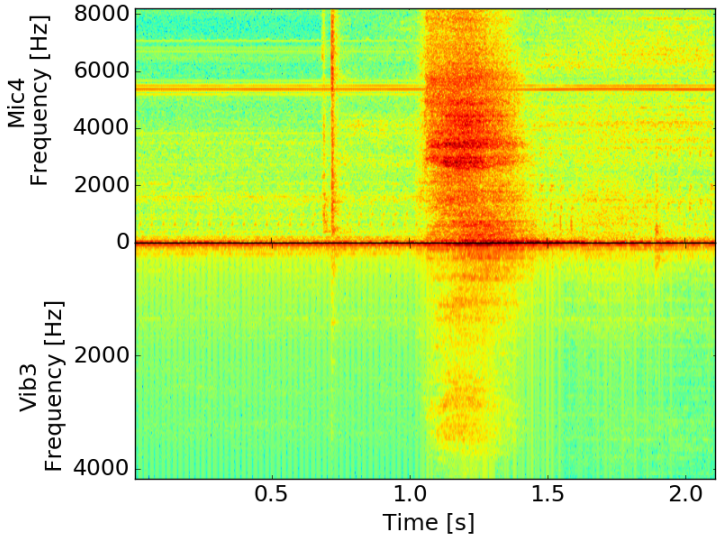

Figure 9: *Waterfall diagram of a four way valve action. The signal in the diagram's upper half was measured by a microphone, the one in the lower half was captured by a vibration sensor. Both types of sensor are suited to allow a fully automatic confirmation of the valve's correct function.*

ing noise sources and sound propagation paths. Figure 10 shows the opening of the expansion valve in the outdoor unit, where it is mounted to the pipes of the refrigerant system. This case is of particular interest, as it was not easily possible to find the source of this signal by human perception alone. Each impulse could be heard in the outdoor chamber, but also traveled over the copper pipes to the indoor unit, where it was heard clearly as well.

The comparison in figure 10 makes clear, that Mic1 (outdoor chamber) must be closer to the signal's source. Furthermore, a possible leakage of aerial sound between the climate chambers could be excluded: The time difference between the two signals is slightly less than 0.01 s. Aerial sound travels about three meters in this time frame. The minimum distance from the possible source to Mic1 and then to Mic2 is at least 6 meters. This leads to the conclusion, that the signal must have traveled along the copper pipes between indoor and outdoor units, which allows for a much faster propagation.

Figure 10 also shows that time and frequency resolution of a waterfall diagram have their limits. For a given sampling rate, the length of the FFT segments determines the resolution: Longer segments increase frequency resolution but decrease time resolution and vice-versa. A strategy to enhance time resolution without sacrificing frequency resolution is to allow overlap

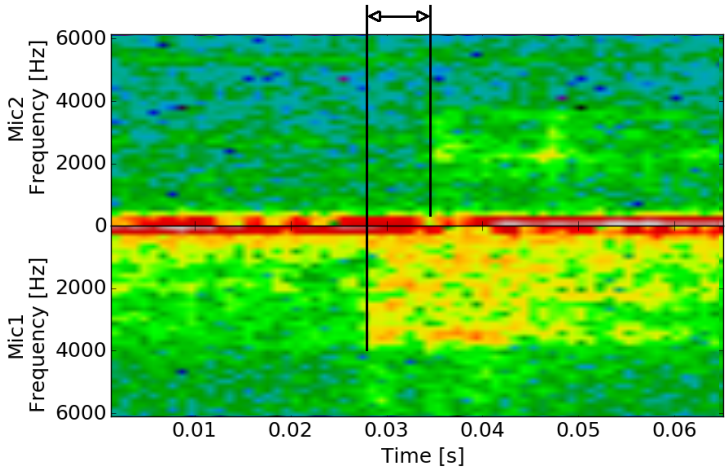

Figure 10: *This click sound by the expansion valve was picked up by one sensor in the outdoor chamber, and one in the indoor chamber. The time shift between these signals is evidence that the signal originated in the outdoor chamber and traveled along the copper refrigerant pipes.*

between adjacent FFT segments. One additional reason to use this strategy is the fact, that all windowing functions typically used in FFT, are heavily center-focused with values decreasing towards the edges. This leads to a focus on the frequency content in the center of the used segment. Partial overlap of the FFT segments helps to reduce the missing-out on frequency content located at the border region between otherwise non-overlapping segments. This is especially important when steep frequency sweeps are present, or when looking for very short transient events.

4.4.4 Fingerprinting

Fingerprinting means to put the heat pump into a defined state of operation and to record its vibration or acoustic spectrum - the fingerprint of the given machine in the given state. This fingerprint can then be used to identify unknown states, or to verify the expected state. An example for the latter would be a part becoming loose or a bearing corroding: The heat pump controller would target a specific operational state, but the vibrational fingerprint would then deviate from the recorded reference. A simple but powerful indicator for machine health.

Figure 11 shows a fingerprint being used for identification. The compressor is decelerating from the 100% power setting to a complete halt. During this

process, it passes through the 69% power state and fingerprinting has been used to find this exact moment. The upper and lower portion of figure 11 show parts of the deceleration process. In between is a snippet of the 69% reference measurement. All major vibrational modes do line up. Differences are due to the fact, that in deceleration the heat pump had no time to equilibrate at the 69% value.

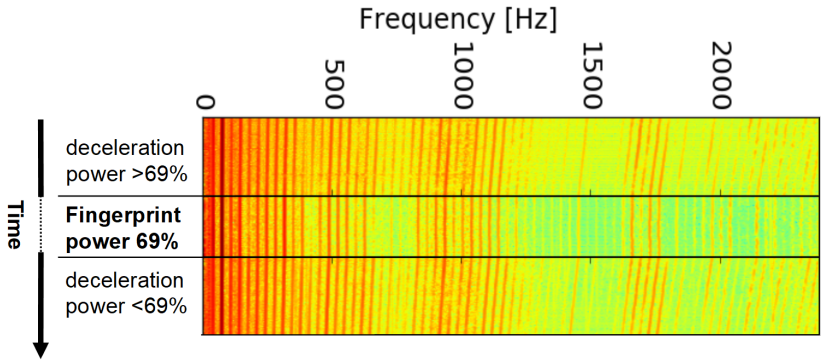

Figure 11: *Top and bottom layer of this figure are taken from a deceleration phase of the heat pump, prior to de-icing. The middle part is a reference fingerprint of a 69% power setting. The exact moment of the heat pump passing through the 69% point was determined by comparing each half second spectrum to the previously measured fingerprint.*

5 Revisiting the commercial heat pump

5.1 Objectives

Goal of this measurement session was to determine the effects of the transition from laboratory situation to deployment on the vibroacoustic characteristics of the heat pump.

5.2 Setup

The instrumentation on the indoor unit is the same as in chapter 4.2 - see figure 2. The outdoor unit was not accessible, so channels Mic1 and Flux were left out.

The heat pump was deployed in a small office, in a "live" environment, where other appliances and third parties within the same building created external noise and vibration, which could not entirely be avoided. Furthermore, these effects slightly varied over time, reducing comparability.

Differences in measured vibration signals are expected to be due to different floor materials, slightly different settings of the heat pump's adjustable feet, and different routing of the refrigerant pipes to the outdoor unit.

Other uncertainties arise from the fact that the temperature difference between the heat pump's inlet and outlet, as well as the mass flow and absolute temperature of the water in the receiving circuit could be monitored, but not adjusted.

5.3 Acoustic environment

As the new location is a small office, the acoustic setting is very different, compared to the acoustically optimized climate chambers. Particularly external background sounds were expected to be an issue.

Figure 12 shows one 38% and one 100% power setting measurement compared to the background measurement with the heat pump turned off. Apart from tonal peaks, the background signal dominates the lower frequency range. Interestingly, in a small range around 520 Hz, the signal-to-background ratio was slightly better than in the climate chambers – see blue and cyan curves in figure 3 and the green difference-inserts in both figures.

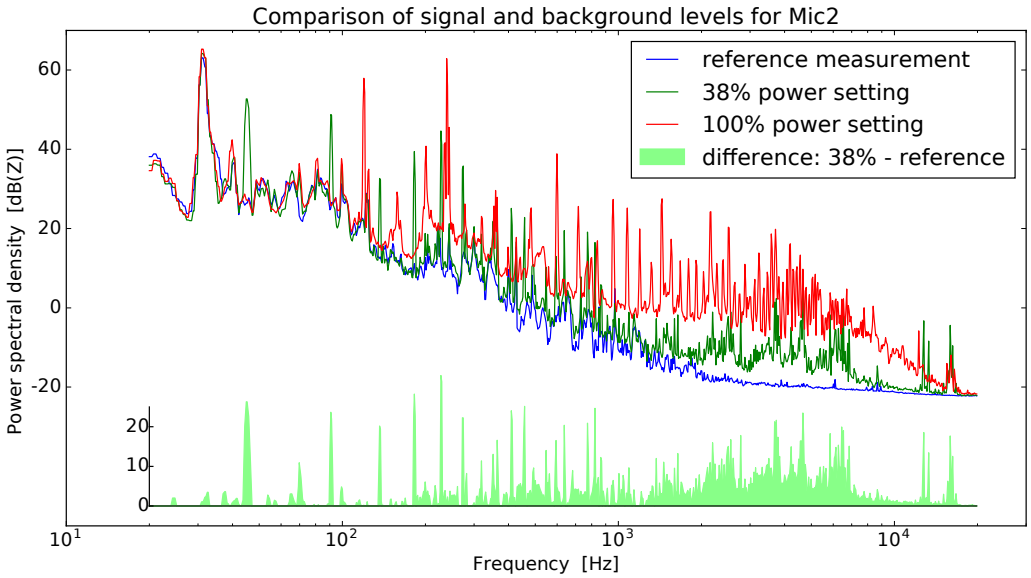

Figure 12: *Comparison of 38%/100% power settings and the reference measurement with the heat pump turned off. The green insert shows the dB-difference between one 38% measurements and the reference signal.*

5.4 Data analysis

Overall, the acoustic measurements the climate chamber and deployment settings are rather similar. In the signals of figure 13, the most prominent newly introduced feature is a broad peak at 30 Hz, which is most probably due to construction works in the same building.

As mentioned in chapter 5.3, the background noise around 520 Hz is lower in the new setting, compared to the climate chambers. This can be directly observed in figure 13, as the signal is effectively lower in the new location.

5.4.1 Peak shift

In figure 14, two small resonance peaks can be seen: At 82 Hz in the lab setting, and at 71 Hz for the new measurements. These peaks can be found in the data of the Vib4 sensor at all power settings. For the 69% power setting the compressor emits vibrations at approximately 80 Hz, resulting in a higher peak for the laboratory configuration, than for the deployment case.

The discovery of the shifted peak shows that the process of uninstalling,

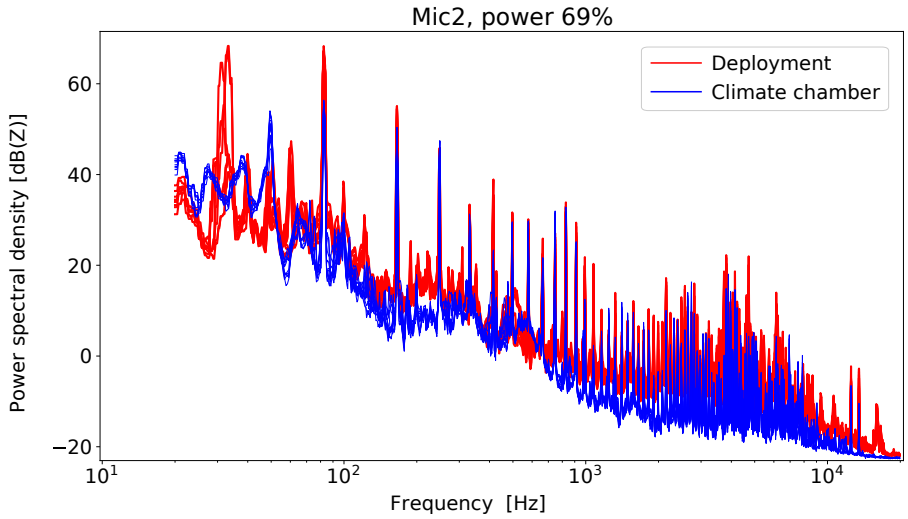

Figure 13: *Comparison between the acoustic signals in laboratory/deployment situations. The strong peak at 30 Hz and its higher harmonics are probably due to construction works in the same building.*

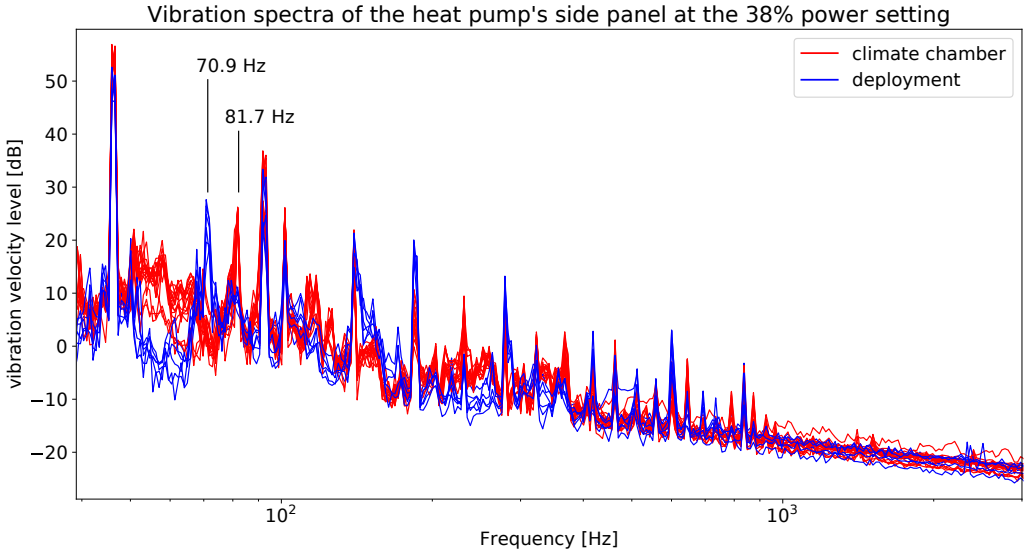

Figure 14: *Comparison of spectra of Vib4 (side panel) at the 38% power setting. A resonance frequency has shifted from 82 to 71 Hz. This leads to decreased vibrations for the 69% power setting.*

transporting and reinstalling a heat pump may also lead to slight alterations of its resonance signature. This can lead to an unpredicted increase in noise

emission, if the new resonance happens to be met by an emission frequency at certain operating conditions. Further more, this has an impact on fingerprinting methods as mentioned in chapter 4.4.4, as the quality of spectral matches is reduced.

6 Measuring acoustic transfer functions

A new Modelica library for combined thermodynamic and acoustic simulation of heat pumps is currently under development by Johann Emhofer (et al.) [15]. It allows the modeled components to have acoustic properties, e.g. the compressor's noise characteristic, with the compressor speed as parameter, as usually supplied by the manufacturer. The goal is not an exact prediction of the noise output of the finished product, but to aid in an active search for optimal sets of configuration parameters to achieve a quieter operation.

As the library does not only consider sound sources, but also allows to model some basic propagation and attenuation processes, detailed measurements of acoustic transfer function of several heat exchangers and acoustic damping materials are needed.

6.1 Objectives

Objective of these measurements was to obtain the acoustic transfer functions of several heat exchangers and damping materials.

The objects and materials examined were:

- a 60x60 cm three-row heat exchanger (short "three-row h-ex")
  25/22/10-3R-24T-600A-4.0PA-3C-Cu/Al/V2A by *WTS Produktion*
- a 50x50 cm five-row heat exchanger (short "five-row h-ex")
  25/22/10-5R-20T-500A-4.4PA-3C-Cu/Al/V2A by *WTS Produktion*
- Cellofoam *Cello D 2600*, 40 mm
- Cellofoam *Cello F800 FR HO ALG-01*, 40 mm
- standard foam black – a thermal/acoustic insulating foam material provided by the AIT

The two heat exchanger units differ in cross-section area and depth (three/five rows of coolant pipes). The materials used and other geometries like fin pitch and shape are identical.

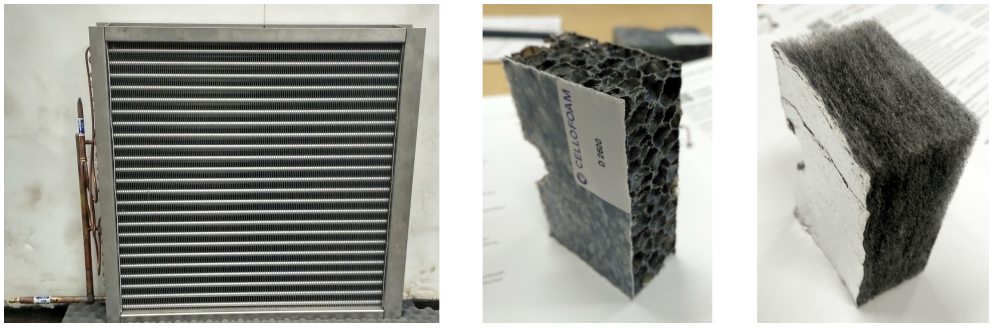

Figure 15: *The three-row heat exchanger (left), and two small samples of Cello D 2600 (middle) and Cello F800 FR HO ALG-01 (right).*

6.2 Setup

For these experiments, the measurement system's input configuration (see chapter 3.2) was reduced to four acoustic channels. One of the two available output channels was used to generate white noise and frequency sweep signals for the transfer function measurement.

The measurements were conducted through an opening between the two ENERGYbase climate chambers (also see chapter 4.2).

The sound absorbing mats were cut to fit the hole. The heat exchangers were smaller than the opening, therefore the remaining gaps were filled with thick layers of standard foam black. For each configuration of the opening (with and without lining by sound absorbing material) reference measurements without sound absorbing mats or heat exchangers were conducted.

6.3 Data analysis

6.3.1 Interference

The microphone Mic1 was positioned between the speaker and the wall opening (see figure 16, right side). When inserting the sound absorbing mat, slight reflections produce standing waves around Mic1, either increasing or decreasing the measured values, depending on the wavelength of the sound in relation to the distance from microphone to mat. This behavior can easily be modeled, allowing to determine the exact distance between mat and microphone.

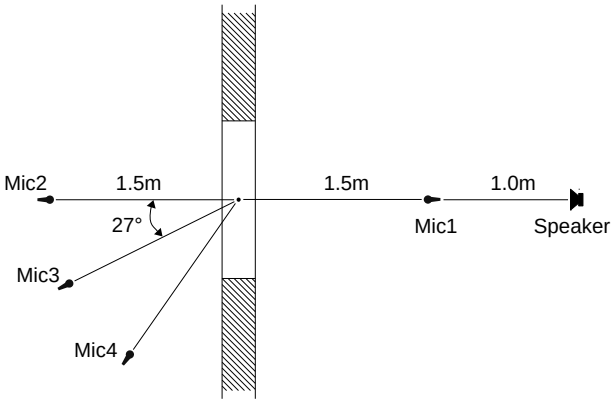

Figure 16: *Top down view of the setup. The sides and top of the wall opening were fitted with standard foam black to accommodate the smaller heat exchangers.*

Figure 17 shows a detail of the spectrum measured at Mic1, compared to the spectrum of numerically simulated interference. This best-fit solution was calculated for a distance of 1.49 m, with a relative intensity of the returning wave of 1.92 %. Given the geometry of figure 16, the primary incident wave has traveled 1 m from the speaker to Mic1, the returning wave traveled 4 m. Using the inverse-square-law and comparing to the fit result, yields an approximate value of 31 % for the acoustic reflectivity of the Cello D 2600 material. This value, of course, is an average over the whole fitted range of the spectrum.

Another interesting feature of figure 17 is the changing amplitude of the numeric solution in the right half of the spectrum. This stems from the fact, that the simulation was done for the same, coarse binning as the original spectrum, which led the interference pattern to violate the Shannon-Nyquist-Theorem in the higher frequency regions. The measured spectrum shows a very similar behavior, further confirming the assumptions and the fit.

6.3.2 Low frequency contamination

During the data evaluation phase it became apparent, that several measurements had been contaminated with external noise in the lower frequency range below 200 Hz. Spectra showed peaks and broadband events, some present in one measurement, vanished in the next. To investigate this problem, overview plots of all measurements were produced. Waterfall diagrams, as mentioned in chapter 4.4.3, were of great help in visualizing and identifying

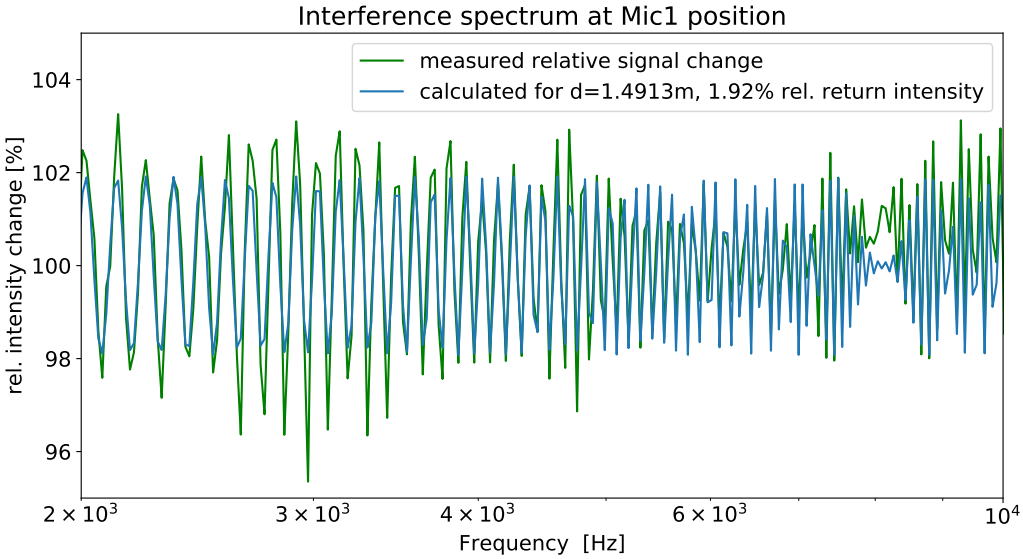

Figure 17: *Detail of the interference pattern in the spectrum of Mic1. The green line is a spectrum of the signal change when inserting the Cello D 2600 material. The fitted cyan line is a simulated interference, indicating a distance microphone to wall of 1.49 m.*

the external contaminations.

An example of such a waterfall overview plot is given in figure 18. The up-down-up movement of the frequency sweep can be seen clearly. But, apart from the first two, all consecutive measurements show defects like the suddenly onsetting lines at 60 Hz and 120 Hz, or a more widespread event between 80 Hz and 150 Hz.

Constant noise lines do not necessarily pose a problem. As long as the transmission measurement and the associated background measurement, are both affected by the same effect, the additional spectral line acts as background noise and is subtracted and therefore canceled.

6.3.3 Comparison of excitation functions

Measurements were carried out with two kinds of sound propagating through the absorbing materials. The first excitation function is white noise. Its fourier transform contains all frequencies, while not having any structure in the time domain, therefore the duration of the signal can be chosen arbitrarily. However, longer signal durations lead to less statistical noise in the resulting

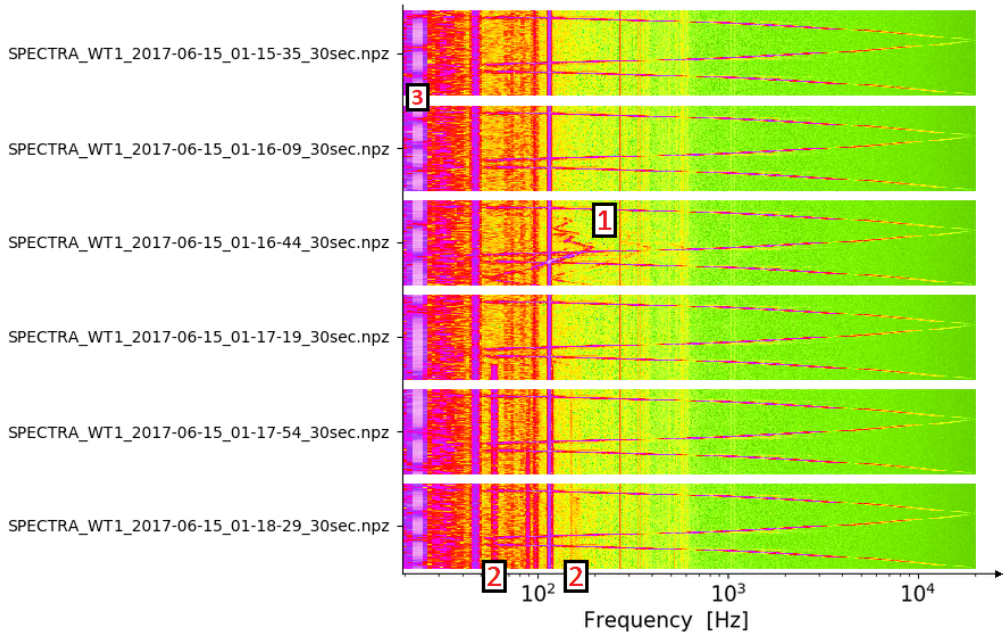

Figure 18: *Visual data inspection with waterfall diagrams of six consecutive sweep measurements, vertical axis is time. The duration of each measurement is 30 seconds. Depicted frequency range is 20 Hz to 20 kHz, logarithmic. Apparent irregularities: (1) localized event, (2) additional spectral lines, (3) intermittent line.*

spectra.

The second excitation function is a frequency sweep. If a sweep's frequency change goes linearly with time, high frequencies will be over pronounced, as it will take the same amount of time to go from 0 to 1 kHz as from 19 to 20 kHz. On the other hand, an exponential frequency increase takes the same amount of time for each octave. In a linear view, as in the FFTs results, which contain linear frequency bins, this leads to a very steep curve in the high frequency region. For the measurements a 4th-order polynomial was chosen which keeps well between these two extremes. This can be observed in figure 18 - an exponential frequency sweep would have led to straight lines, without the slight curvature.

Figure 19 shows spectra of both types of signals. Though having the same amplitude during numeric waveform generation, the sweep signal yields a much higher signal-to-background ratio. It lies consistently 12-25 dB above the white noise signal. This is especially valuable in the lower frequency regions: Above 150 Hz, the white noise signal starts to separate significantly

from the climate chamber's background noise. Due to the higher SNR, the sweep signal is already usable from 30 Hz on.

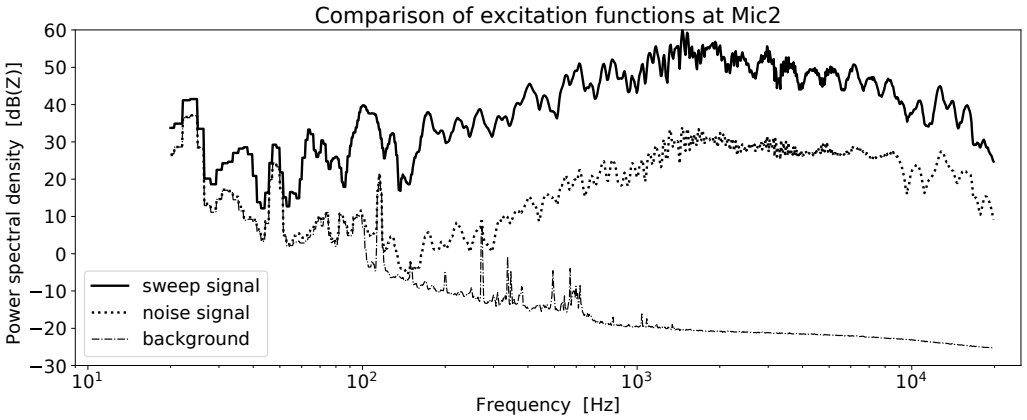

Figure 19: *Measured spectra at the Mic2 position, without absorbing material. With equal amplitude during signal synthesis on the computer, the sweep function results in a much higher signal at the receiver side.*

6.3.4 Background subtraction

Using the data obtained with sweep and noise signal measurements, the spectral transmission will be calculated in this manner:

$$\frac{signal_{transmitted} - background}{signal_{reference} - background} = transmission \tag{2}$$

This calls for a way to subtract the background spectrum from a signal. As no coherence between the signals can be assumed, the differences have to be calculated quadratically:

$$\sqrt{p_{signal}^2 - p_{background}^2} = p \tag{3}$$

Using levels in decibel units, this calculation changes further to:

$$10 \cdot log_{10}\left(10^{\frac{L_{p,signal}}{10}} - 10^{\frac{L_{p,background}}{10}}\right) = L_p \tag{4}$$

Equation 3 already hinted at the problem of negative values, when a background signal is higher than the respective sweep/noise measurement. This

can happen due to statistical errors or external noise contamination. In equation 4, even equal values of associated levels lead to problems in calculation of the logarithmic function.

Also, when signal and background are very close, this leads to the logarithm function being very steep, largely amplifying any statistical noise.

Figure 20 shows the effects of background subtraction. For this example, data from the Cello D 2600 absorber was chosen as this resulted in the lowest signal levels of all tested materials. Due to the high signal strength, the sweep measurement remains virtually unaffected by the background subtraction. On the other hand, below 170 Hz the noise signal is greatly changed.

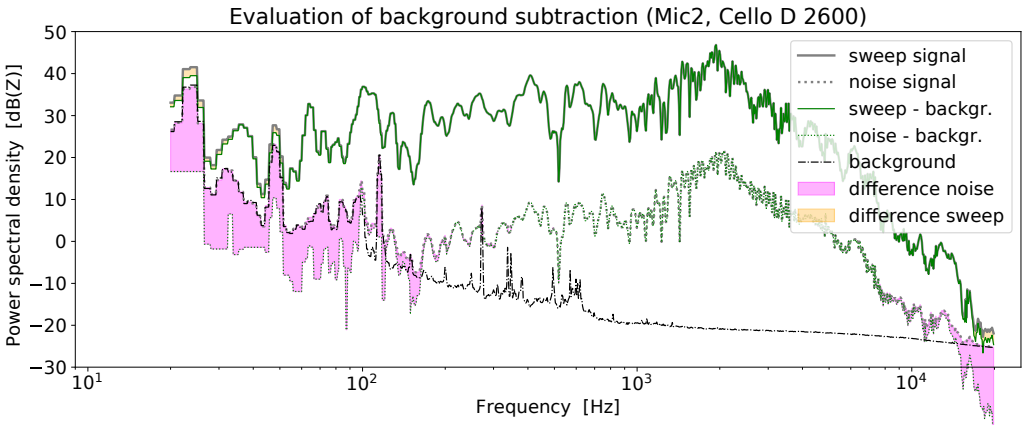

Figure 20: *Measured spectra at the Mic2 position, with the Cello D 2600 sound absorbing material in place. Orange and pink areas highlight the differences of the respective signals when background is subtracted. Due to the high signal strength, the sweep measurements are virtually unaffected by the subtraction.*

Figure 20 also implicitly shows the chosen way of interpolation in cases where the background signal is higher: If an invalid value is encountered, the last valid value is repeated. This leads to the *flat bottom* artifacts, as seen at the lowest frequencies of the noise signal measurement (lower end of the pink area in figure 20).

6.3.5 Extracting background information from sweep measurements

As seen in chapter 6.3.4, background signals only have a small effect on the sweep measurements. For the white-noise measurements or other scenarios,

with less speaker output power, or a material with higher damping values, the effects of the background subtraction increase significantly. Furthermore, as seen with the low frequency contamination in chapter 6.3.2, the possibility of a changing background environment makes a close time relation between transmission measurement and background measurement desirable.

In the sweep measurements of figure 18 it is obvious, that for each moment in time, only a very small portion of the spectrum is used for the actual transmission measurement. All other parts of the spectrum are purely governed by the background noise. This information can be harvested and assembled to a complete background spectrum.

The most simple approach is to take the upper half of the spectrum in the exact moment, when the sweep is at its lowest frequency, and do so vice-versa with the lower half.

Another approach exploits the fact, that the actual sweep occupies each part of the spectrum only for a short amount of time. Using the same procedure as for the waterfall diagrams - calculating the FFTs of short slices of the recording - the median value for each frequency bin leads to the background level. Due to the amount of background values compared to the high but few sweep values, the median is guaranteed to lie within the scatter width of the background levels, but will exhibit a slight bias upwards of the true background average value. The main advantage of this second approach lies in the fact that no information about the exact timing of the sweep is needed.

Figure 21 compares the background spectrum extracted from a sweep measurement to a traditionally measured spectrum. The match is very good, all differences are below 1 dB.

The use of sweep measurements to provide the background spectrum information also carries the advantage that the traditional background measurements can be omitted, which greatly reduces overall measurement time.

6.3.6 Binning and power spectral density

The calculation instruction of equation 2 applies to each frequency bin separately, and is therefore independent of the chosen binning. The fast fourier transform (FFT) yields spectra in linear binning. The count of elements of a given array and its sampling frequency determine the bin width after applying FFT. As the frequency perception of human hearing is better described logarithmically, linear binning is rather coarse for lower frequencies

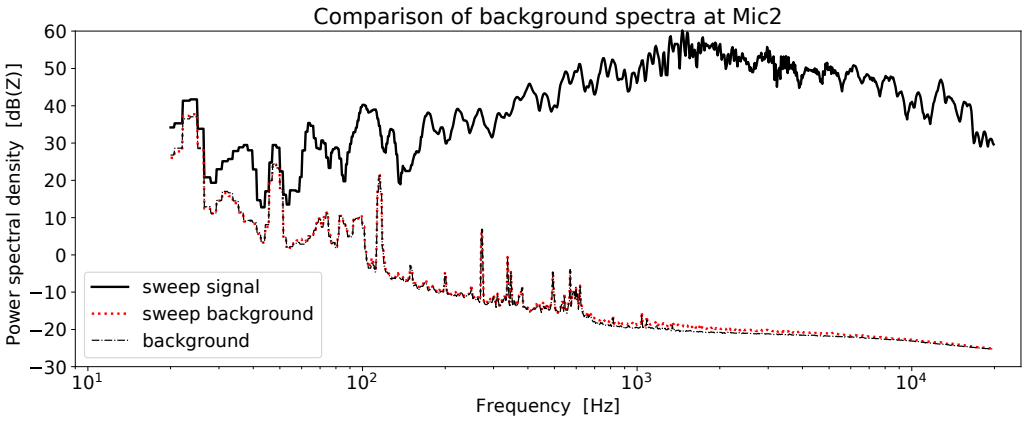

Figure 21: *Measured spectra at the Mic2 position, without absorbing material. The background signal extracted from the sweep measurement is very close to the traditional background measurement.*

and very fine grained in the higher regions. As already mentioned in chapter 4.4.3, shorter FFT segments increase time resolution, which is important for waterfall diagrams, but also aids in the extraction of the background signal "between" a frequency sweep as demonstrated in chapter 6.3.5.

To better represent human hearing, the spectra were re-binned to a logarithmic frequency scale, with exponentially growing bin width. For a smooth plot a resolution of at least 1000 points is desirable. Given the range of human hearing from 20 Hz to 20 kHz, this leads to the first, and most narrow bin to have a width of 0.13 Hz. A signal of length 2^{14} (16384 samples), at 48 kHz sampling rate, has a duration of $\approx \frac{1}{3}$ second, and therefore a frequency resolution of 3 Hz. At high frequencies, several linear bins are merged to one logarithmic bin. But at low frequencies, the logarithmic resolution is higher than the linear, which causes one linear bin to be distributed to several logarithmic bins. This results in a staircase effect, which can be seen below 100 Hz in figures 20 and 21. Equal resolution for these parameters (1000 logarithmic bins, 2^{14} linear bins) is reached at 422 Hz.

A problem for all re-binning procedures is that the represented signal stays the same, but the displayed bin-content changes. Combining two or more bins is done by adding the respective values, as the total power in the spectrum's integral has to be preserved. As bins in a logarithmic scale widen with a factor of two with each octave, this addition results in a slope of +3 dB per octave. Also changing the total amount of bins, like reducing 1000 to 500 bins by always combining two adjacent bins, leads to an increase of +3 dB

for the whole spectrum.

To eliminate the spectrum's dependence of the chosen binning, a conversion is done from Pa^2 to Pa^2/Hz. This leads to the *power spectral density* (PSD) [16]. Now bin width cancels out, as doubling width results in -3 dB, but adding both bins' signals (similar values assumed) results in +3 dB, giving no shift or slope over the whole spectrum.

For a given binning, this conversion from a power spectrum to power spectral density is a constant factor (additive in dB) for each bin - the reciprocal bin width. In decibel units:

$$L_{p,f}[\mathrm{dB_{SPL}}] + 10 \cdot log_{10}(\tfrac{1[\mathrm{Hz}]}{b_f[\mathrm{Hz}]}) = L_{p,f}[\mathrm{dB_{PSD}}] \tag{5}$$

b ... bin width
f ... denoting the bin with center frequency f

With transfer functions in view, this leads to no changes: From equation 5 follows that a difference (in dB units) of two power spectra or two PSD spectra cancels out the newly introduced bin width factor, leading to equal results.

On a side note, this is also the same reason, why weighting functions (e.g. A-weighting) were not taken into account for calculating transfer functions, as these would cancel out.

6.3.7 Representation of the transfer functions

The transfer functions were calculated in high resolution (1000 bands, logarithmic) and then re-binned for octave bands and third-octave bands. These standardized formats aid in comparability and easier handling of the functions by greatly reducing the number of data points. A side-by-side comparison of the different resolutions can be seen in figures 22 and 23.

Detailed figures and tabulated values for all measured transfer functions can be found in the appendix, chapter 10.1.

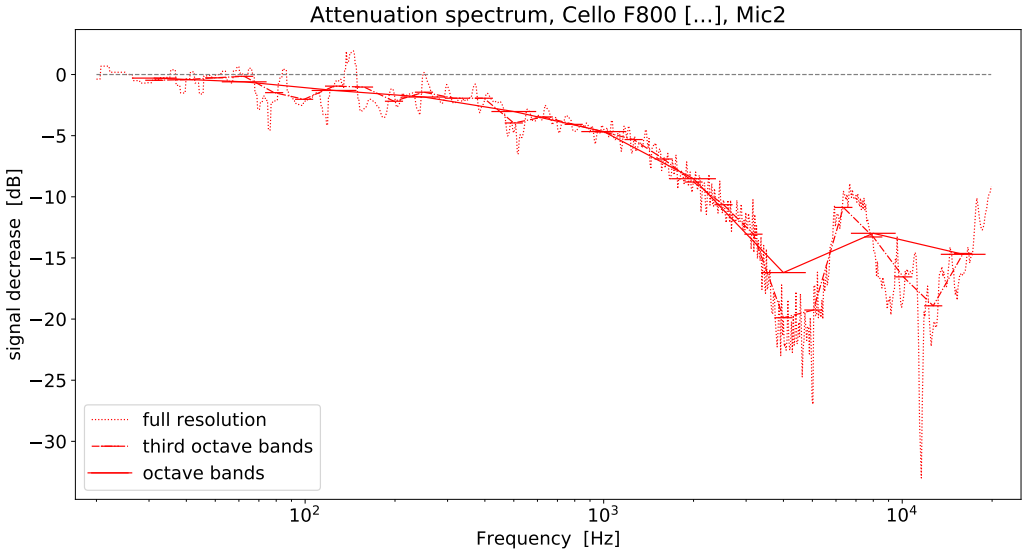

Figure 22: *Acoustic transfer function of Cello F800 FR HO ALG-01. A narrower binning carries more information about the transfer function at the cost of a higher data handling complexity.*

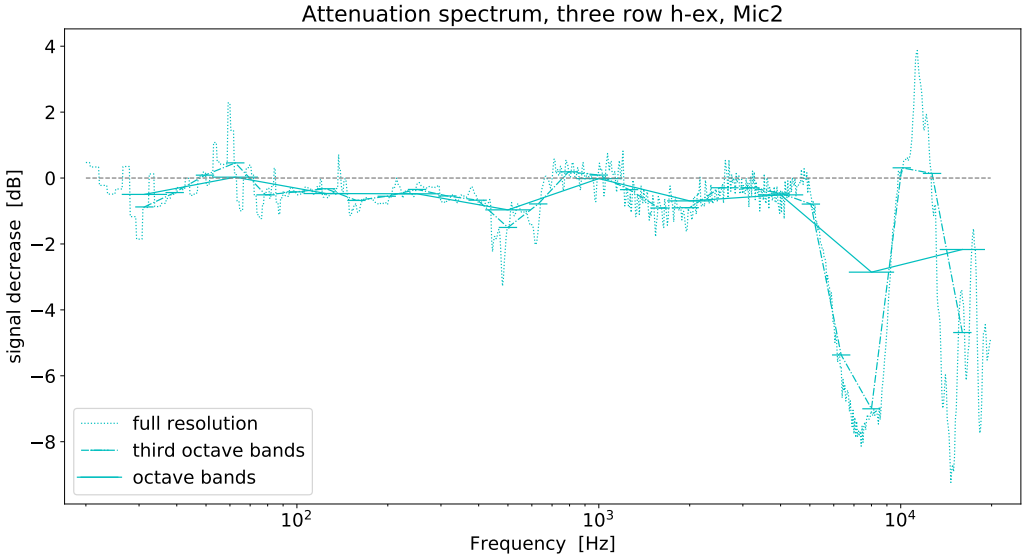

Figure 23: *Acoustic transfer function of the three-row heat exchanger. The strong attenuation values around 7-8 kHz coincide with elevated reflection values detected at Mic1 (not shown here).*

7 Acoustic transfer functions with air flow

7.1 Objectives

In chapter 6 the transfer functions of several materials and heat exchangers were determined. For a sound absorbing mat, these results can be used directly. Heat exchangers, on the other hand, are subject to air flow along the sound propagation direction. This could alter the transfer function, or introduce new aero acoustic contributions to the noise spectrum.

The objects examined were (see chapter 6.1):

- 60x60cm three-row heat exchanger
- 50x50cm five-row heat exchanger

7.2 Setup for measurements with air flow

Compared to the setup in chapter 6.2, several alterations had to be made to provide air flow for the heat exchangers. Direct fan attachment was not possible as the fan's noise would strongly affect the measurements. To minimize these effects, the fan was placed outside of the climate chambers, and a flexible sound-insulated air duct was used to guide the flow into the chamber, to the wall opening and the heat exchanger.

All components were arranged around a second opening between the chambers, which was smaller and on floor level. This was necessary, to be able to directly connect the air duct. A round-to-square adapter box was constructed from cardboard with inner and outer layers of sound absorbing material. The speaker was placed on the bottom of this box, in a slightly upward facing manner - see figure 24.

The tilted speaker and this newly introduced resonance chamber lowered the accuracy of the measured transfer functions. However, this did not decrease the value of this setup as its primary goal was to qualitatively investigate the existence of any airflow-induced influence on the heat exchangers transfer function.

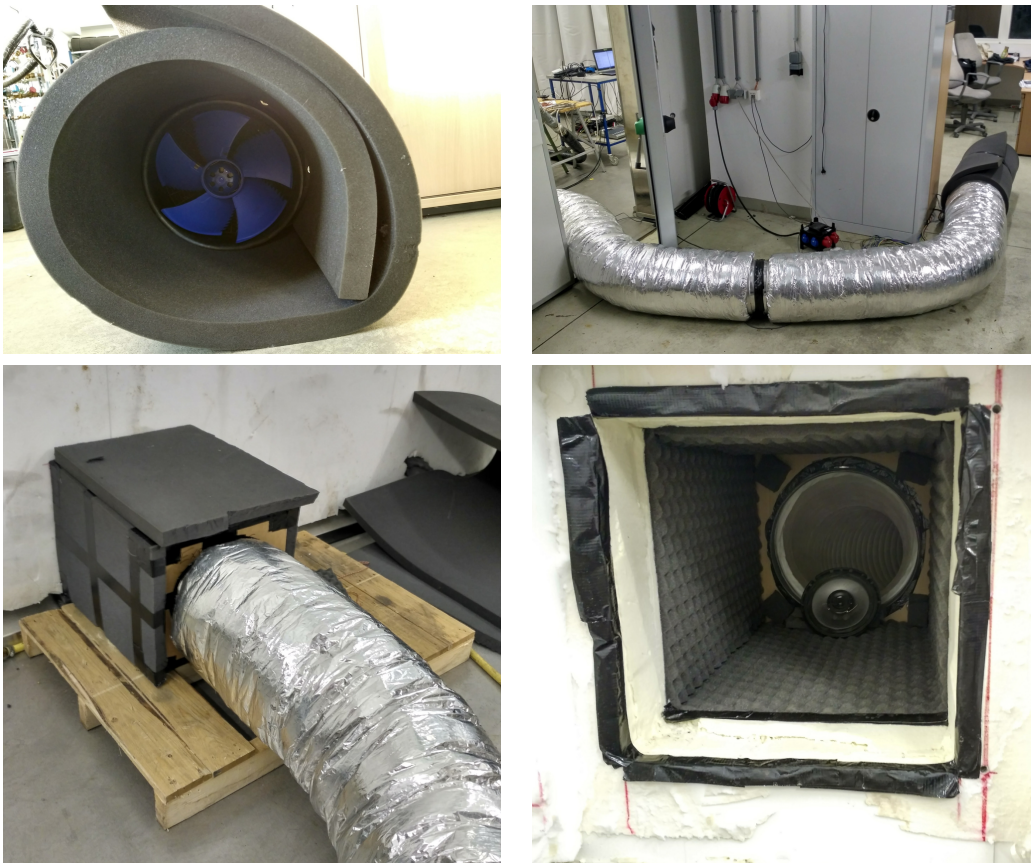

Figure 24: *Path of the air flow. Top left: Fan, rolled up into a thick piece of sound absorbing material. Top right: Flexible insulated air duct, entering the climate chamber. Bottom left: Round-to-square adapter box, with sound absorbing material on inside and outside. Bottom right: Wall opening, seen from the second climate chamber.*

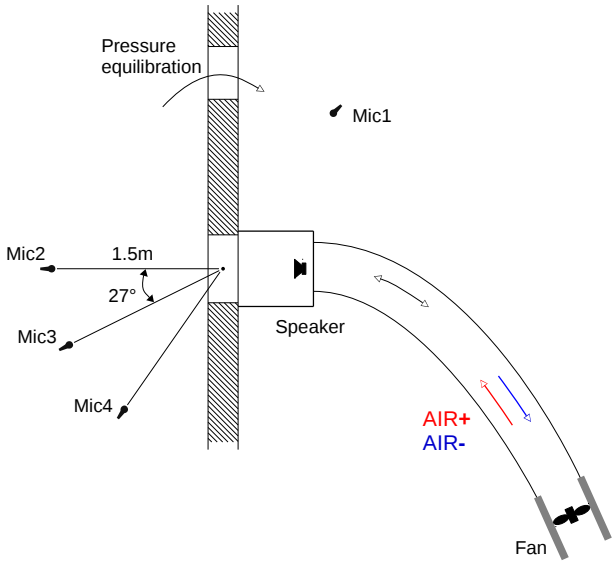

Figure 25: *Top down view of the setup. The outer walls and doors of the climate chambers were omitted in this drawing. The fan was further away than this drawing suggests. Refer to figure 24 for a more accurate impression of the air path.*

7.3 Data analysis

7.3.1 Wind speed

The fan was controlled by a pulse width modulated signal, which does not translate linearly into rotation speed. Three different parameter values (40%, 70% and 100%) were chosen to be measured, in both positive (in direction of sound propagation) and negative directions. For negative air flow speeds, the fan had to be manually reversed.

Throughout this chapter, fan settings are denoted by "AIR", followed by a sign to indicate flow direction and three digits, indicating the selected percentage parameter, e.g. AIR+040 (see figure 25).

For each combination of fan setting and heat exchanger the wind speed was measured with a hand held anemometer, at a fixed distance from the wall opening. Only for outward air flow velocities were measured. Inward air flow is not directed at the probe, leading to significantly lower measurements for the same fan settings. The values determined are listed in the table below.

	air velocity [m/s]		
fan setting [%]	five-row h-ex	three-row h-ex	**w/o** h-ex
100	1.52	1.34	3.98
070	1.20	1.11	3.03
040	0.67	0.58	1.69
000	0.00	0.00	0.00

Air velocities at 30 cm distance from the wall opening, measured for different fan settings and heat exchangers.

7.3.2 Resonances

The round-to-square adapter box (see figure 24) unavoidably acts as a resonance chamber. This introduces resonant behavior, which increases with room mode density towards higher frequencies. In figure 26 resonances can be seen above 1 kHz. These resonances also strongly affect the determination of transfer functions as can be seen in figure 27.

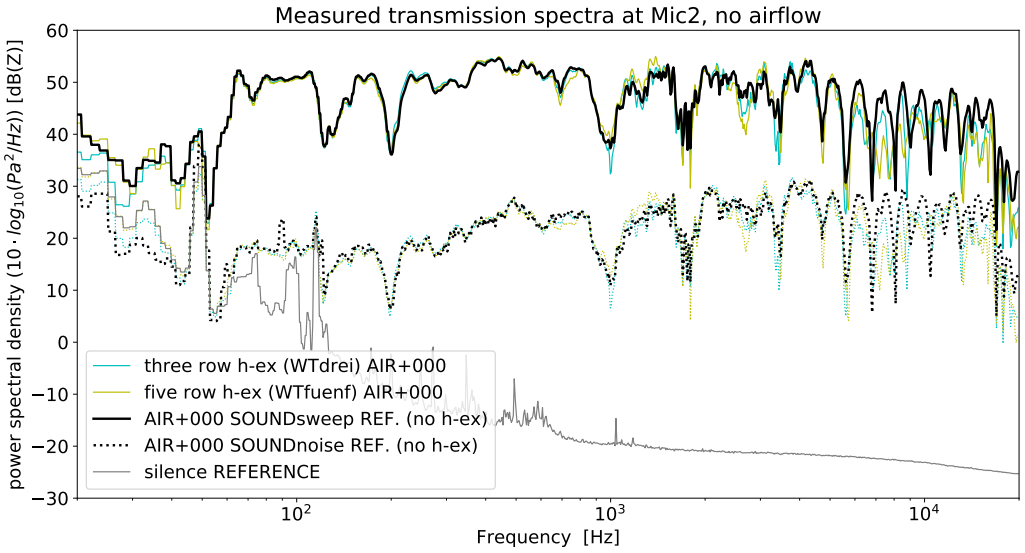

Figure 26: *Measured spectra at the Mic2 position, without air flow. Reference signals without heat exchanger are shown in black, colors indicate the used heat exchanger. Both, white noise (dashed) and sweep (continuous lines) signals show strong resonances above 2 kHz. These are introduced by the rectangular adapter box between air duct and wall opening.*

7.3.3 Air flow artifacts

Figure 27 shows transmission spectra of the five-row heat exchanger at different wind speeds. Most prominent feature of this figure is the apparently very strong noise reduction below 100 Hz for the measurements with positive air flow direction. This artifact is a result from Mic2 being located in the direction of the air stream. During the reference measurement without heat exchanger the air flows past Mic2, resulting in low frequency wind noise. With the heat exchanger in place, this flow is strongly reduced, leading to artificially high attenuation values in the respective frequency range.

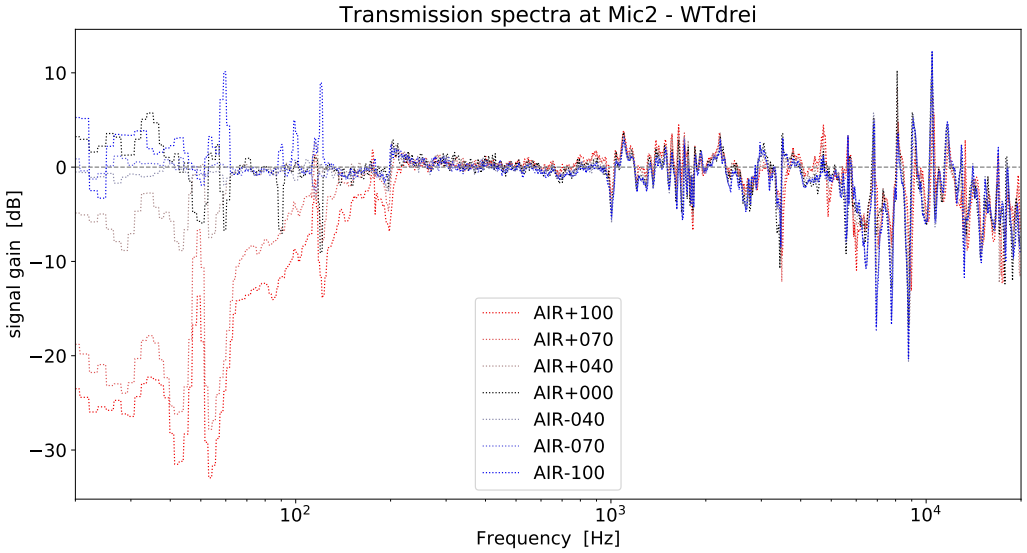

Figure 27: *Transmission spectrum of the three-row heat exchanger at the Mic2 position. During reference measurements with positive air flow direction, Mic2 is directly affected by the flow, which causes the major artifacts below 200 Hz. Above 1 kHz resonances from the adapter box distort the transfer functions.*

7.3.4 Aero acoustic effects

The aero acoustic spectra were calculated with the same procedure as transmission spectra, one measurement with heat exchanger in place divided by one without heat exchanger. The difference is that the speaker was turned off - therefore the designation "silence". This results in a spectrum of only aeroacoustic effects - and possibly the damping of any residual fan noise which was not eliminated by the extensive insulating ductwork.

Figure 28 shows such spectra. Mic4 was chosen as this microphone is farthest away from the air flow and therefore has the cleanest reference measurements. The most prominent feature of this graph is the large bulge of the AIR+100 curve at 2 kHz. Also, several smaller features between 400 Hz and 1 kHz can be seen. All of them, with varying intensity, can also be found in the AIR+070 curve. The curves with negative air flow direction (higher pressure on the side of the microphones) do not show this behavior.

To give an exact number for the sound volume of the bulge at 2 kHz, several quantities have to be summed: The value of the background signal, the peak value of the bulge (see fig. 28), the bin width factor of the respective bin to convert from PSD to power spectrum (see chapter 6.3.6), and the A-weighting factor.

$$-15.4\text{dB(Z)}_{backg.} + 6.2\text{dB}_{bulge} + 17.2\text{dB}_{binning} + 1.2\text{dB}_{A-wgt} = 9.2\text{dB(A)}$$

A value of 10 dB(A) is commonly compared to leaves rustling in the distance, which means that it could be heard in an otherwise completely silent room, but will easily be drowned out by any other noise. In a similar calculation, the bulge at 450 Hz yields 11.8 dB(A) - and everything below is greatly reduced by the A-weighting curve. Therefore, these effects will not contribute significantly to the noise load for wind speeds in the range measured.

Another obvious feature of figure 28 are the sharp spikes of the AIR+100 curve at 176 Hz and higher harmonics. These spikes are related to the rotation frequency of the fan at the 100% setting: When placing the heat exchanger in front of the wall opening, the pressure within the air duct slightly rises, which in turn causes the fan to slow down. A subtraction of these two very close peaks then leads to the apparent sharp upwards-downwards peak structure, leaving them as artifacts in the graph. Less pronounced, this can also be seen in the AIR-100 curve - which additionally shows external contamination below 70 Hz.

7.3.5 Air flow effects on the acoustic transfer functions

To estimate the extent of the air flow effects on the transfer functions, the actual transfer functions and resonance effects have to be deducted from the spectra in figure 27. The transmission spectra for the AIR+000 setting do contain exactly this – all acoustic transfer and resonance effects, but no

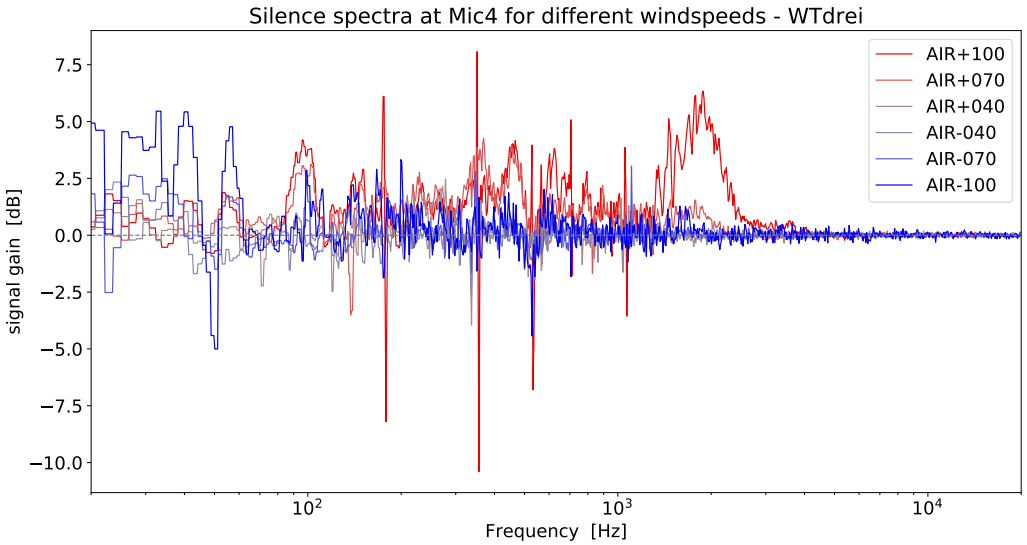

Figure 28: *Aero acoustic spectra of the three-row heat exchanger without any sound input. The large bulges of the curves with positive air flow direction have been identified as aero acoustic noise effects. The sharp spikes, as well as the features below 70 Hz, are artifacts.*

air flow during measurements. Therefore, a further quotient of spectra is introduced:

$$\frac{Tr_{AIR\pm xxx}}{Tr_{AIR+000}} = AE_{AIR\pm xxx} \tag{6}$$

Tr ... transmission spectrum for specific air flow
AE ... air flow effect

Transmission spectra are calculated according to equation 2. Equation 6 simplifies to a subtraction when used in decibel units. Results of this calculation can be seen in figure 29.

The full resolution curve in figure 29 shows that the influence of resonances still could not be fully mitigated with this approach. As the application of a rather broad binning has a strong averaging effect, the use of third-octave and full octave bands eliminates the up-down-run of the curve. This reveals the net influence of the air flow – for octave bands a change of up to 3.0 dB for the air flow speeds measured.

Third-octave and octave spectra also exhibit a strong flow speed and direction dependence: The effect is much more pronounced when air and sound travel

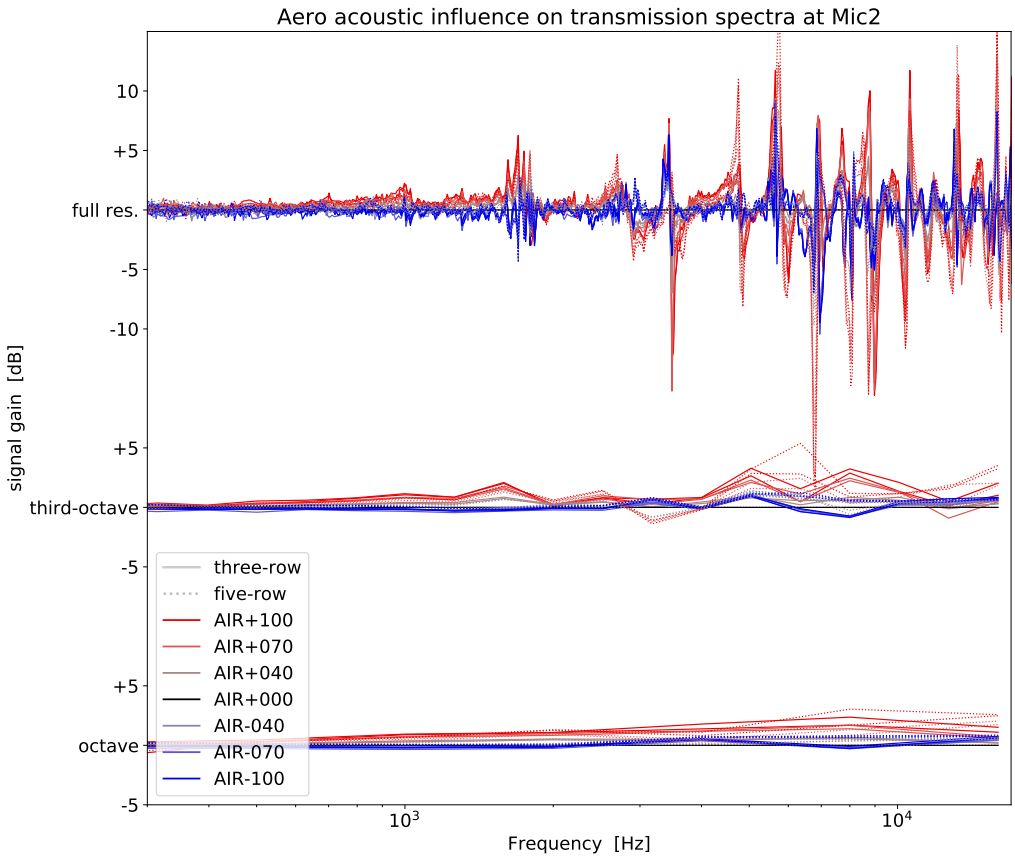

Figure 29: *Spectra of the air flow influence on the transmission functions, with different binnings. The line style (dotted/continuous) indicates the heat exchanger used. Note that the frequency range in this figure starts at 300 Hz.*

in the same direction (AIR+ settings). Furthermore, the effect scales with flow speed.

To gain better knowledge about the actual frequency dependencies of the air flow effect, further measurements with an improved, resonance-reduced setup are needed.

8 Summary

In the course of this thesis, a modular multichannel measurement system has been constructed. Complete with software and ready-to-use scripts for data acquisition, this system has proven to be a useful tool in the development and improvement of heat pumps or similar equipment.

The simultaneous acquisition of multiple signals of very diverse sources helps to investigate the relations between them. Separate systems would need a very high effort in timekeeping to achieve a similar degree of simultaneousness.

Various approaches of data evaluation have been demonstrated - some taking advantage on single calibrated channels, whereas others exploit the high simultaneousness of the signals. Visualization of data and data products is key for understanding and interpreting the results. Several different approaches have been used to convey as much information as possible, while keeping the diagrams still easy to comprehend.

The measurement system has been put to practical use in several different cases. A commercially available heat pump was examined in detail, producing useful feedback for the manufacturer and showcasing the measurement system's strengths at its planned area of use. These results have been presented at the DAGA 2017 conference in Kiel, Germany [18].

Acoustic transfer functions of several different materials were measured and will be incorporated in the Modelica SSElib. Additionally, first steps were taken to quantify the effects of air flow on the aeroacoustic transfer functions of heat exchangers.

Results from this thesis have also been incorporated in further research activities and were presented at various locations and conferences [19] [20] [21] [22].

9 References

[1] D. J. Wuebbles, D. W. Fahey, K. A. Hibbard, et al.: *Climate Science Special Report: Fourth National Climate Assessment, Volume I*, U.S. Global Change Research Program, Washington, DC, USA, 2017.

[2] D. Schäuble, D. Volkert, D. Jacobs, K. Töpfer: *CO_2-Emissionsgrenzwerte für Kraftwerke – Ausgestaltungsansätze und Bewertung einer möglichen Einführung auf nationaler Ebene*, Institute for Advanced Sustainability Studies (IASS), Potsdam, April 2014.

[3] M. Reichart, A. Sauer: *Gebäude*, in: *Energieeffizienz in Deutschland – eine Metastudie* (A. Sauer, T. Bauernhansl, ed.), 2nd Edition, Springer Vieweg, Berlin, 2016.

[4] C. Maschke, A. Jakob: *Psychoakustische Messtechnik*, in: *Messtechnik der Akustik* (M. Möser), Springer-Verlag, Berlin, 2010.

[5] G. F. Hundy, A. R. Trott, T. C. Welch: *Refridgeration, air conditioning and heat pumps*, Fifth Edition, Elsevier, Oxford, 2016.

[6] T. Nowak, P. Westring: *European Heat Pump Market and Statistics Report 2016*, European Heat Pump Association AISBL (EHPA), Brussels, 2016.

[7] Ch. Reichl: *SilentAirHP Schallreduktion für Luftwärmepumpen*, in: *energy innovation austria* 3/2016, Bundesministerium für Verkehr, Innovation und Technologie, Wien, 2016.

[8] N. Schmiedbauer, J. Emhofer, C. Köfinger, P. Wimberger, T. Fleckl, M. Gröschl, Ch. Reichl: *Aktive Störschallunterdrückung für Wärmepumpenanwendungen*, 43. Jahrestagung für Akustik, Kiel, Deutschland, 06.-09. März 2017.

[9] P. Wimberger, J. Emhofer, C. Köfinger, T. Fleckl, M. Gröschl, Ch. Reichl: *Space-, time- and frequency resolved recording and analysis of sound emissions and sound source localisation using a multichannel measuring system*, 66. Jahrestagung der Österreichischen Physikalischen Gesellschaft, Wien, 27.09.2016.

[10] P. Cladé: *PyDAQmx: a Python interface to the National Instruments DAQmx driver*, http://pythonhosted.org/PyDAQmx/, accessed 09/2016.

[11] R. Kern: *A Simple File Format for NumPy Arrays*, SciPy.org, 20.12.2007.

[12] LOUD Technologies Inc.: *MACKIE. 1202-VLZ3 Owner's Manual*, Woodinville WA, USA, 2006.

[13] Mackie Designs Inc.: *MACKIE. 1202-VLZ PRO specification sheet*, Woodinville WA, USA, 2003.

[14] W. Nitsche, A. Brunn: *Strömungsmesstechnik*, 2. Auflage, Springer-Verlag. Berlin, Heidelberg, 2006.

[15] J. Emhofer, R. Zitzenbacher, Ch. Reichl: *Sound Source Extension Library for Modelica*, in: *Proceedings of the 12th International Modelica Conference, May 15-17, 2017, Prague, Czech Republic*, (Jirí Kofránek, Francesco Casella, editors), Linköping University Electronic Press, 2017.

[16] R. B. Randall: *Frequency Analysis*, 3rd edition, Brüel & Kjær, Nærum, Denmark, 1987.

[17] Physikalisch-Technische Bundesanstalt Braunschweig und Berlin: *PTB-Mitteilungen, Fachorgan für Wirtschaft und Wissenschaft*, Heft 2, 117. Jahrgang, Juni 2007, Wissenschaftsverlag NW, Verlag für neue Wissenschaft, Bremerhaven, 2007.

[18] F. Linhardt, K. Alten, J. Emhofer, C. Köfinger, T. Fleckl, P. Wimberger, M. Gröschl, Ch. Reichl: *Charakterisierung der Schallabstrahlung von Luft-Wasser-Wärmepumpen mittels simultaner Hitzdrahtanemometrie, Vibrationsmessung und Schalldruckbestimmung*, 43. Jahrestagung für Akustik, Kiel, Deutschland, 06.-09. März 2017.

[19] Ch. Reichl, J. Emhofer, P. Wimberger, N. Schmiedbauer, F. Linhardt, E. Wasinger, C. Köfinger, T. Fleckl: *SilentAirHP - Analyse und Entwicklung von Schallreduktionsverfahren für Luft-Wasser-Wärmepumpen*, 43. Jahrestagung für Akustik, Kiel, Deutschland, 06.-09. März 2017.

[20] Ch. Reichl, M. Popovac, E. Wasinger, D. Meisl, R. Zitzenbacher, F. Linhardt, J. Emhofer: *Icing of heat exchangers investigated by measurements and simulations on micro- and macroscale*, 25th ERCOFTAC Alpe Danube Adria Pilot-Center Meeting & ERCOFTAC Spring Festival 2017, AIT, Austria, 06.04.2017.

[21] Ch. Reichl, M. Popovac, E. Wasinger, D. Meisl, R. Zitzenbacher, F. Linhardt, P. Wimberger, N. Schmiedbauer, J.

Emhofer, M. Gröschl: *Experimental and numerical methods for the fluid dynamic and acoustic characterization of heat exchanger icing*, Jahrestagung der österreichischen und Schweizer physikalischen Gesellschaft, 21.-25. August 2017, Genf (CERN und CIGG).

[22] Ch. Reichl, J. Emhofer, M. Popovac, P. Wimberger, F. Linhardt, K. Alten, T. Fleckl: *IEA HPT Annex 51: Acoustic Signatures of Heat Pumps Update - Acoustic Transmission Measurements and Sound Source Detection*, 26th ERCOFTAC Alpe Danube Adria Pilot-Center Meeting, TU Graz, Austria, 24.10.2017.

10 Appendix

10.1 Transfer functions

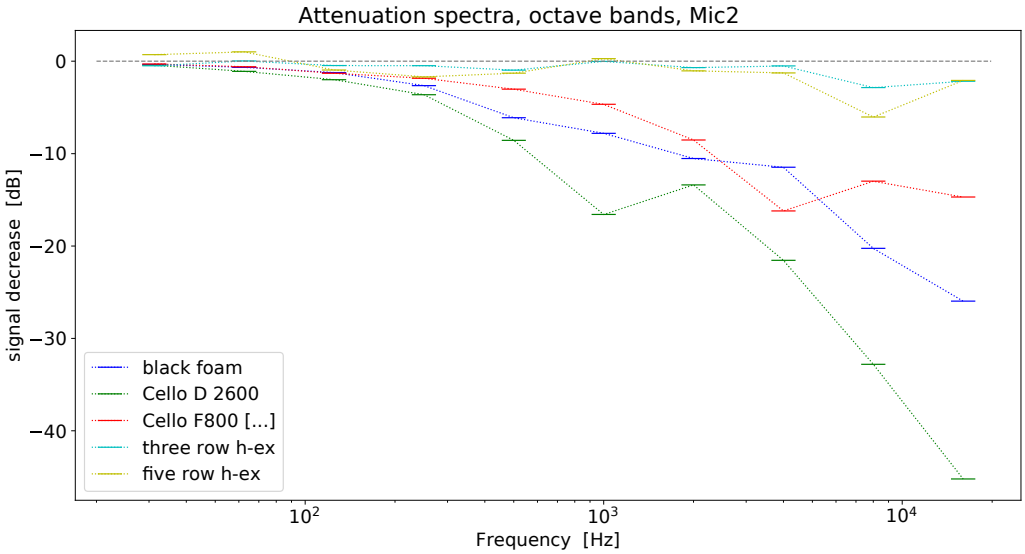

Figure 30: *Transmission spectra in octave band resolution.*

Freq.	black foam	Cello D 2600	Cello F800 [...]	three-row	five-row
31.25	-0.26	-0.45	-0.34	-0.48	0.70
62.50	-0.79	-0.92	-0.47	0.13	0.77
125	-1.22	-2.08	-1.27	-0.48	-1.13
250	-2.64	-3.62	-1.83	-0.48	-1.71
500	-6.12	-8.55	-3.03	-0.96	-1.32
1000	-7.81	-16.59	-4.67	-0.01	0.27
2000	-10.54	-13.38	-8.52	-0.69	-1.06
4000	-11.48	-21.53	-16.17	-0.50	-1.29
8000	-20.28	-32.82	-12.99	-2.84	-6.06
16000	-25.98	-45.21	-14.70	-2.15	-2.11

Attenuation values for different materials in octave band resolution, as depicted in figure 30. Frequencies in Hz, attenuation values in dB.

Freq.	black foam	Cello D 2600	Cello F800 [...]	three-row	five-row
19.69	-0.20	-0.15	0.63	0.60	-1.29
24.80	-0.73	-0.17	0.03	-0.21	0.93
31.25	0.37	-0.33	-0.56	-0.87	1.47
39.37	-0.54	-0.89	-0.51	-0.37	-0.56
49.61	-0.61	-0.57	0.05	0.10	1.51
62.50	-0.58	-1.10	-0.36	0.91	1.31
78.75	-1.19	-1.12	-1.19	-0.76	-0.90
99.21	-1.50	-2.75	-1.87	-0.48	-0.90
125	-0.46	-1.24	-0.92	-0.32	-0.87
157	-1.85	-2.42	-1.08	-0.66	-1.67
198	-2.84	-3.76	-2.13	-0.54	-1.60
250	-1.87	-2.78	-1.47	-0.36	-1.22
314	-3.37	-4.54	-1.94	-0.54	-2.41
396	-4.34	-5.58	-1.94	-0.68	-2.14
500	-7.96	-10.87	-3.97	-1.51	-0.92
629	-6.95	-12.34	-3.46	-0.76	-0.98
793	-6.98	-15.16	-4.08	0.19	0.66
1000	-7.49	-17.16	-4.70	0.10	0.44
1259	-9.29	-17.90	-5.31	-0.34	-0.35
1587	-11.15	-15.25	-6.91	-0.90	-1.32
2000	-11.92	-11.27	-8.79	-0.89	-1.09
2519	-9.03	-14.90	-10.65	-0.29	-0.79
3174	-7.77	-19.65	-13.04	-0.29	-0.84
4000	-13.96	-21.40	-19.87	-0.45	-1.23
5039	-23.12	-25.23	-19.18	-0.78	-1.85
6349	-24.66	-29.09	-10.89	-5.37	-6.10
8000	-18.15	-36.62	-13.28	-6.98	-12.62
10079	-20.35	-39.02	-16.53	0.32	-3.48
12699	-23.71	-42.70	-18.90	0.15	-0.95
16000	-27.48	-47.62	-14.62	-4.67	-3.63

Attenuation values for different materials in third octave band resolution, as depicted in figure 31. Frequencies in Hz, attenuation values in dB.

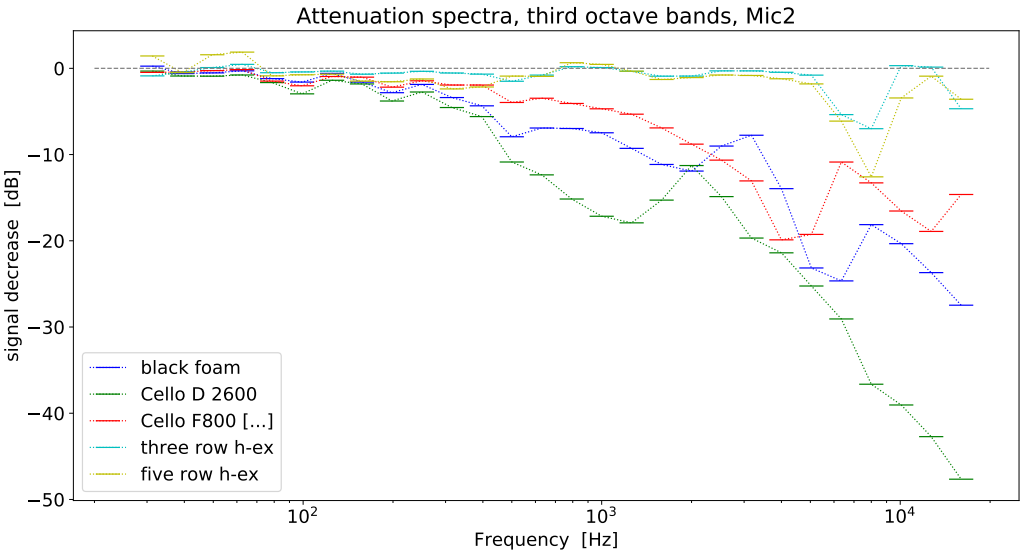

Figure 31: *Transmission spectra in third octave band resolution.*

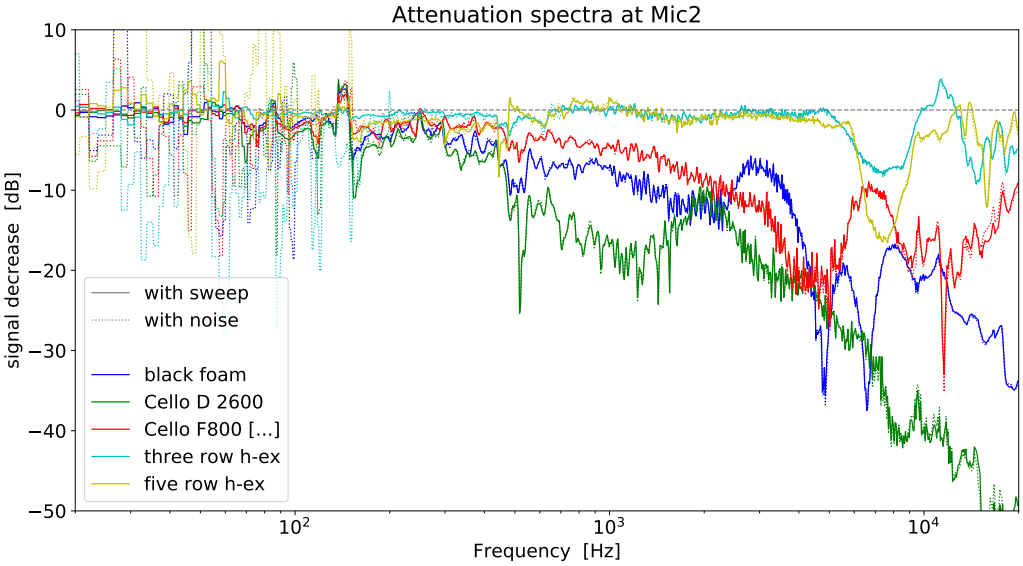

Figure 32: *Transmission spectra in full resolution.*

10.2 Contribution at DAGA 2017

The following pages include the contribution to the DAGA 2017 conference proceedings. An oral presentation was given in context of the DAGA track "Lärmentstehung und -ausbreitung".

Charakterisierung der Schallabstrahlung von Luft-Wasser-Wärmepumpen mittels simultaner Hitzdrahtanemometrie, Vibrationsmessung und Schalldruckbestimmung

Felix Linhardt[1,2], Karoline Alten[3], Johann Emhofer[1], Christian Köfinger[1],
Thomas Fleckl[1], Peter Wimberger[1], Martin Gröschl[2], Christoph Reichl[1]

[1] *AIT Austrian Institute of Technology, Center for Energy,*
[2] *TU Wien, Institut für Angewandte Physik,*
[3] *AIT Austrian Institute of Technology, Center for Mobility,*
E-Mail: felix.linhardt.fl@ait.ac.at

Einleitung

Am Beispiel einer Luft-Wasser-Wärmepumpe wurde die gleichzeitige Messung von punktuellen Strömungsgeschwindigkeiten, Vibrationen und orts- und frequenzaufgelöste Schalldruckpegeln zur spektralen Charakterisierung herangezogen. Die Messungen wurden in einer akustisch optimierten Klimakammer durchgeführt, um auch die transienten Vorgänge bei der Vereisung des Verdampfers beobachten zu können. Dabei wurde die Strömung lokal mittels eines Hitzdrahtanemometers bestimmt, das eine Analyse der Strömungsgeschwindigkeiten sowie der Turbulenzspektren ermöglichte. Die Vibrationen wurden durch piezoelektrische Schwingbeschleunigungssensoren erfasst, die mittels Magnethalterungen an maßgeblich schwingenden Komponenten der Wärmepumpe montiert waren. Aufgrund ihres geringen Gewichts von nur 54g und ihres breiten Frequenzbereiches (0.1 - 4800 Hz) eignen sie sich gut für derartige Schwingungsmessungen ohne eine rückkoppelnde Wirkung auf das Messobjekt auszuüben. Im Postprocessing wurden die Daten integriert, um die Schwingschnelle für die weitere Berechnungsschritte zu erhalten. Die Messung der Schalldruckpegel erfolgte ortsaufgelöst mittels 1/2 Zoll Klasse 1 Messmikrofonen. Neben der herkömmlichen Charakterisierung durch Vergleich von Schwingungs-, Strömungsturbulenz- und Schalldruckspektren wurde durch die zeitgleiche Messung der Signale eine zusätzliche zeitliche Korrelation der Signale möglich, die weitere Rückschlüsse auf die Signalzusammenhänge ermöglicht.

Anwendungsziele

Der vorliegende Messaufbau stellt einen wichtigen Schritt in Richtung zweier Zielsetzungen dar. Einerseits sollte ein Werkzeug entwickelt werden, das es Wärmepumpenherstellern erlaubt, im Zuge der Entwicklung und des Prototypenbaues, die Auswirkungen konstruktiver Veränderungen am Gerät auf einfache Weise nachzuvollziehen und bewerten zu können.

Andererseits handelt es sich dabei auch um Voruntersuchungen, ob und wie ein kontinuierliches Machine-Health-Monitoring auf Basis von Schall-, Vibrations-, und Strömungsmessungen realisiert werden kann.

Messkette

Die vier Akustikkanäle, vier Vibrationskanäle, und der Strömungskanal generieren Signale, die über jeweilige Verstärkereinheiten auf einer Messkarte zusammengeführt werden. Diese Messkarte gestattet das Abtasten aller Kanäle mit bis zu 96 kHz. Via USB-Schnittstelle werden die Daten auf den Computer übertragen (Schema in Abbildung 1).

Der Softwarestack besteht aus den Hardwaretreibern des Herstellers und dazu passenden Python-Bindings. Damit ist dann die gesamte Funktionalität direkt aus Python heraus ansteuerbar.

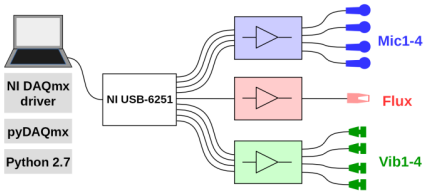

Abbildung 1: Die Signale der neun Sensoren werden über jeweils spezifische Verstärker an eine Datenerfassungskarte geführt. Der Softwarestack besteht aus den Hardwaretreibern des Herstellers, die direkt mit Python angesteuert werden können.

Wärmepumpe und Messbedingungen

Für die Testmessungen stand eine kommerzielle Luft-Wasser-Wärmepumpe zur Verfügung. Es handelt sich dabei um ein Split-Gerät, mit Ventilator und Verdampfer in der Außeneinheit und, unter anderem, Kompressor, Umwälzpumpe und einem Warmwasserspeicher in der Inneneinheit (siehe auch Abbildung 2). Die Leistung konnte für die Messungen als fixe Größe vorgegeben werden. Angefahren wurden 20% als Minimalwert, der Nennleistungspunkt von 38%, und weiters 69% sowie 100%. Zu jeder Leistungseinstellung wurden für die Außeneinheit auch verschiedene Klimabedingungen zwischen +7°C und -7°C vorgegeben, sowie für die Inneneinheit unterschiedliche Vor- und Rücklauftemperaturen.

Je nach Klima- und Leitungsvorgaben kam es zu Vereisung am Verdampfer, wodurch Abtauungsvorgänge notwendig sind, die automatisch ausgelöst oder manuell geschaltet werden konnten.

Um eine konstruktive Veränderung am Innengerät zu simulieren, wurde jede Messung je einmal mit geschlossener sowie geöffneter Fronttüre der Wärmepumpe durchgeführt.

Sensorpositionen

Von den neun Sensoren wurden ein Mikrofon und der Strömungssensor in der Klimakammer mit dem Außengerät aufgestellt, die verbleibenden drei Mikrofone und die vier Vibrationssensoren wurden beim Innengerät angebracht (siehe Abbildung 2).

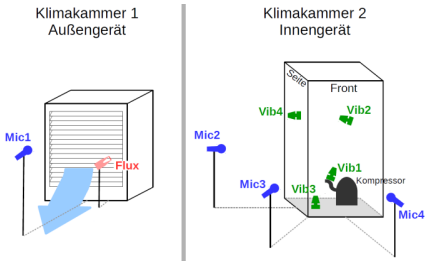

Abbildung 2: Am Außengerät wurde an der Ausblasseite Strömung und Schalldruck (Mic1 außerhalb der Strömung) gemessen. Das Innengerät wurde mit vier Vibrationssensoren und drei Mikrofonen vermessen. Sensor Vib1 sitzt dabei an einer Kältemittelleitung in der Nähe des Kompressors. Vib2 wurde an der Innenseite der Fronttüre platziert.

Untersuchung zeitlicher Mittelwerte

Durch zeitliche Mittelung lassen sich für die einzelnen Sensorkanäle sehr leicht handhabbare Maßzahlen errechnen. Über die freien Parameter der Leistungsvorgabe und der Türstellung können damit Aussagen über die Zusammenhänge einzelner Kanäle getroffen werden.

Für die Akustikkanäle wird der Dauerschallpegel verwendet, die Vibrationskanäle werden durch den Effektivwert (quadratischer Mittelwert) der Schwingschnelle charakterisiert. Der Strömungskanal kann in diesem Kontext sowohl durch den Mittelwert charakterisiert werden, der ein Maß für die Effektivströmung darstellt, als auch durch die Standardabweichung, die als Maß für die Turbulenz der Strömung herangezogen wird.

Beispiel 1: Mic4 gegen Vib3 (Abbildung 3)
Sensor Vib3 befindet sich auf der inneren Bodenplatte des Innengeräts, Mic4 direkt frontal davor. Mit dem Anheben der Wärmepumpenleistung ist ein deutlicher Anstieg in den Vibrationswerten zu beobachten, der auch stark mit dem Anstieg des Schalldruckpegels korreliert. Das Öffnen der Fronttüre führt zu einem vibrationsunabhängig weiteren Ansteigen des Schalldruckpegels um bis zu 10dB.

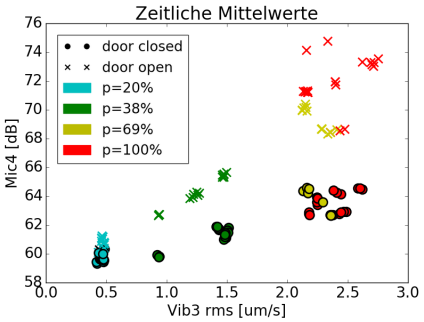

Abbildung 3: Mic4 (Innengerät, frontal) gegen Vib3 (Bodenplatte). Beim Vergleich dieser beiden Sensoren, zeigt sich bei Erhöhung der Kompressorleistung ein stetes Ansteigen der Vibrationen, in starker Korrelation mit dem Schalldruckpegel. Deutlich sichtbar ist auch die Dämpfungswirkung der geschlossenen Wärmepumpentüre.

Beispiel 2: Mic2 gegen Vib4 (Abbildung 4)
Besonders auffällig ist bei Sensor Vib3, dass bei einer Leistung von 38%, jedoch nur bei geschlossener Fronttüre, ein deutliches Maximum in der Vibrationsstärke erreicht wird. Dies deutet auf Resonanzeffekte in der Seitenwand hin, deren Anregungsfrequenzen über die Fronttüre übertragen werden.

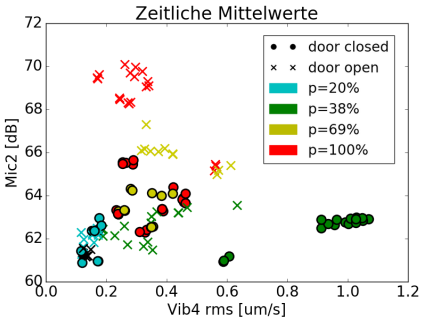

Abbildung 4: Mic2 (Innengerät, Seite) gegen Vib4 (Seitenwand). Sensor Vib4 zeigt hohe Effektivwerte bei Leistung 38%. Diese treten jedoch nur bei geschlossener Fronttüre auf, was auf Einkopplung der entsprechenden Frequenzen über die Türe hinweist.

Bei der Leistungseinstellung 38% liegen auch die Schallpegel an Mikrofon Mic2 bei geöffneter Türe größtenteils unter den Messungen bei geschlossener Türe. Dies zeigt sich jedoch nicht in den Kanälen Mic3 und Mic4 (hier nicht im Bild), sodass gefolgert werden kann, dass die gemessenen Vibrationen auch mit Richtwirkung von der Seitenwand akustisch abgestrahlt werden.

Beispiel 3: Mic1 gegen Flux Standardabweichung (std-dev), entspricht der Turbulenz (Abbildung 5)
Bei diesen Messungen der Außeneinheit zeigt sich, dass eine Minderzahl der Messpunkte deutlich erhöhte Turbulenz- sowie damit verbundene Schalldruckpegelwerte aufweisen. Weitere Recherche in den Metadaten dieser Messungen zeigt, dass diese Aufnahmen jeweils kurz vor einem automatisch ausgelösten Abtauungsvorgang stattfanden. Dies bedeutet, dass der fortgeschrittene Vereisungsgrad des Verdampfers mit einer deutlichen Turbulenz- und Schalldruckpegelzunahme einher geht.

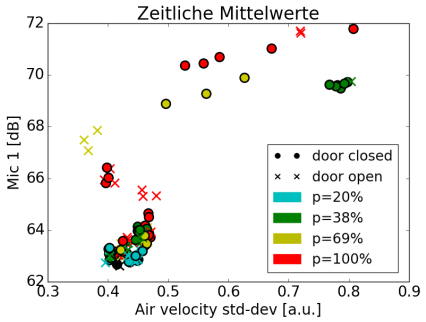

Abbildung 5: Mic1 gegen Flux (std-dev, Turbulenz).
Die Messungen mit besonders hohen Turbulenz- und Schalldruckpegelwerten beim Außengerät, fallen mit fortgeschrittener Vereisung am Verdampfer zusammen.

Kreuzkorrelation der Zeitreihen

Durch die gleichzeitige Messung aller neun Kanäle ist es möglich, die Kreuzkorrelationsfunktion zwischen je zwei Kanälen zu bilden. Da es sich um Zeitreihen handelt, bekommt der freie Parameter der Kreuzkorrelationsfunktion die Bedeutung eines Zeitversatzes. Um den verschiedenen möglichen Schallwegen Rechnung zu tragen, wird der untersuchte Parameterbereich für den Zeitversatz derart gewählt, dass die längste im Messaufbau vorkommende Abmessung noch von Luftschall im gegebenen Zeitfenster in die eine oder andere Richtung zurückgelegt werden kann. Aus diesem eingeschränkten Parameterbereich wird das Maximum der Kreuzkorrelationsfunktion als Übereinstimmungsmaß herangezogen. Daraus ergibt sich für jede Messung zwischen allen Kanälen eine symmetrische Kopplungsstärkematrix (siehe Abbildung 6).

In allen solchen Kopplungsstärkematrizen zeigt sich, dass das Strömungssignal nicht an die anderen Signale koppelt – die Korrelationswerte liegen bei 10^{-3} bis 10^{-5}. Grund dafür ist, dass das Strömungssignal Ähnlichkeit zu einem rosa Rauschen aufweist, und daher über längere Zeitreihen hinweg sich keine Korrelation zu den anderen, tonaleren Signalen zeigen kann.

Bei der Betrachtung der Kopplungsstärke zwischen Vibration und Akustik zeigen sich bei niedrigen Leistungseinstellungen gleichmäßig geringe Korrelationswerte. Bei hoher Wärmepumpenleistung (siehe Abbildung 6) zeigen besonders die kompressornahen Vibrationssignale Vib1 und Vib3 starke Korrelation mit den Mikrofonsignalen, wohingegen die Anteile von Vib2 und Vib4 abnehmen.

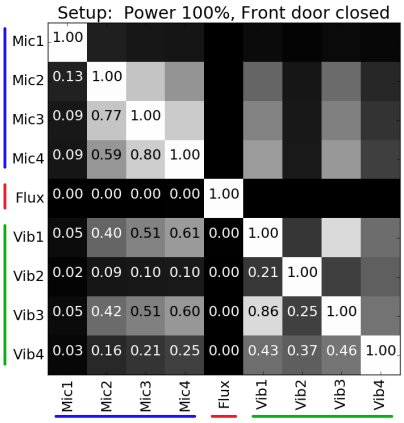

Abbildung 6: Die Einträge der Kopplungsstärkematrizen werden über die Kreuzkorrelationsfunktion gebildet. Für die Leistungseinstellung 100% mit geschlossener Fronttüre zeigt sich, dass die Vibrationssignale von Sensor Vib1 (Kompressorzuleitung) und Vib3 (innere Bodenplatte) sich deutlich in den Mikrofonsignalen Mic2-4 abzeichnen. Das Strömungssignal ist weitestgehend ein Rauschsignal und korreliert daher kaum mit den anderen, tonaleren Signalen.

Untersuchung transienter Ereignisse

Die gleichzeitige und hochfrequente Erfassung aller Kanäle erlaubt, auch transiente Ereignisse mit mehreren Sensoren zu untersuchen. Eine Erfassung solcher Ereignisse kann insbesondere bei Prototypen hilfreich sein, um Schallwege nachzuvollziehen, oder um dann im Regelbetrieb die erfolgreiche Ausführung eines Steuerbefehls zu überwachen.

Beispiel 4: Öffnen des Expansionsventils (Abbildung 7)
Im Außengerät befindet sich ein Expansionsventil, dessen kurzes Öffnungsgeräusch mit Mikrofonen beider Klimakammern nachgewiesen werden kann. Es zeigt sich auch ein Zeitversatz, der bestätigt, dass sich die Quelle des Signals in der Außenkammer befinden muss. Wichtigster Schallübertragungsweg dürften die kupfernen Kältemittel-

leitungen gewesen sein, die Innen- und Außengerät verbinden.

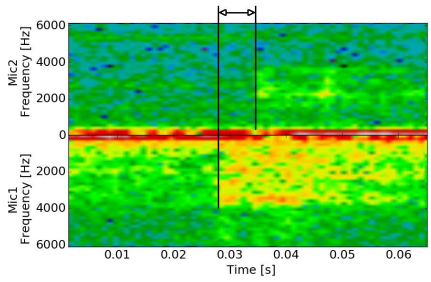

Abbildung 7: Öffnungsgeräusch des Expansionsventils am Außengerät. Sowohl Mic1 (Außen-Klimakammer) als auch Mic2 (Klimakammer des Innengeräts) haben das Ereignis detektiert. Der Zeitversatz zeigt, dass sich die Signalquelle in der Außenkammer befinden muss.

Beispiel 5: Umschalten des 4-Wege-Ventils (Abbildung 8)
Beim Einsetzen einer Abtauphase wird, nachdem der Kompressor heruntergefahren wurde, der Kältemittelkreislauf umgekehrt. Dies geschieht über ein 4-Wege-Ventil. Dessen gesamter Schaltvorgang – zu Beginn ein Klicken, ein Expansionsgeräusch, und ein Klick am Ende – kann sowohl mit den Vibrationssensoren als auch den Mikrofonen mitverfolgt werden.

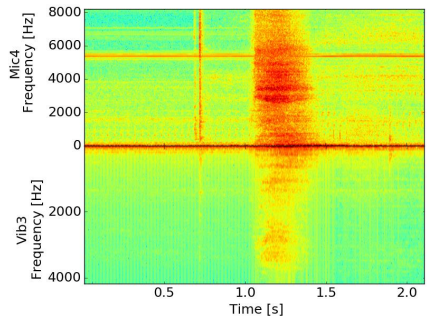

Abbildung 8: Schaltvorgang des 4-Wege-Ventils am Beginn einer Abtauphase. Sowohl akustisch (Mic4) als auch vibrationssensorisch (Vib3) lässt sich dieses Ereignis detektieren und mitverfolgen. Deutlich zeichnen sich Beginn (0.7s) und Ende (1.9s) der Ventilbewegung ab. Dazwischen findet sich das Expansionsgeräusch des Kältemittels.

Fingerprinting von Betriebszuständen

Einzelne Leistungszustände der Wärmepumpe gehen mit einer bestimmten Kompressordrehzahl einher, und besitzen dadurch sehr charakteristische spektrale Fingerabdrücke. Solche Fingerabdrücke können bei bekannten Betriebszuständen genommen werden, um unbekannte Zustände zu identifizieren.

Beispiel 6: Herunterfahren des Kompressors (Abbildung 9)
Zu Beginn einer Abtauphase muss zunächst der Kompressor heruntergefahren werden. Dabei durchläuft er innerhalb von zwei Minuten alle Drehzahlzustände unterhalb des Startzustandes. Daher findet sich auch der spektrale Fingerabdruck des 69%-Leistung-Zustandes in dieser Drehzahlrampe.

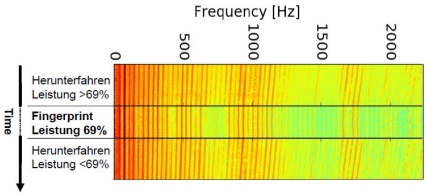

Abbildung 9: Der obere und untere Bereich sind aufeinanderfolgende Ausschnitte aus dem Herunterfahren des Kompressors. Mittig zu passendem Zeitpunkt eingefügt, ist der spektrale Fingerabdruck des 69%-Leistung-Zustandes dargestellt.

Zusammenfassung

Es wurde ein Messsystem entwickelt, das es erlaubt, auf einfach Weise eine konstruktive Änderung im Hinblick auf Schall- und Vibrationsverhalten zu bewerten. Die gleichzeitig hohe Abtastrate aller Kanäle erlaubt auch Untersuchungen der Kopplungsstärke zwischen den einzelnen Kanälen.

Als Testfall eines konstruktiven Eingriffs wurde der Öffnungszustand der Fronttüre herangezogen, womit schon deutliche Änderungen im Vibrations- und Schallverhalten induziert wurden.

Für ein Continuous Machine Health Monitoring wurde gezeigt, dass Betriebszustände anhand ihrer spektralen Fingerabdrücke identifiziert werden können, und dass sowohl Mikrofone als auch Vibrationssensoren transiente Ereignisse überwachen können.

Danksagung

Das Projekt SilentAirHP wird im Rahmen des Energieforschungsprogramms des Klimaenergiefonds (5148527) in einer Initiative des österreichischen Bundesministeriums für Verkehr, Innovation und Technologie gefördert.